



July 15, 1991

N00140-88-0677

Investigation of Hot Streak Migration and Film Cooling Effects on the Heat Transfer in Rotor/Stator Interacting Flows

Quarterly Technical Progress Report For
April 1 through June 30, 1991

Prepared for NAVAIR

by

Daniel J. Dorney and Roger L. Davis
Theoretical & Computational Fluid Dynamics
United Technologies Research Center

DTIC
ELECTE
JUL 31 1991
S D D

Introduction

The specific objectives of this effort are to extend the NASA-Ames Rai [1, 2] three-dimensional rotor/stator interaction code, ROTOR3, to investigate hot streak migration and film cooling effects on the passage flow and blade surface heat transfer for an axial flow turbine stage. These objectives are part of an overall plan to extend the capabilities of this numerical procedure and to determine the potential of this technique to impact the design of future rotating turbomachinery components.

The principal benefits that will result from this effort are:

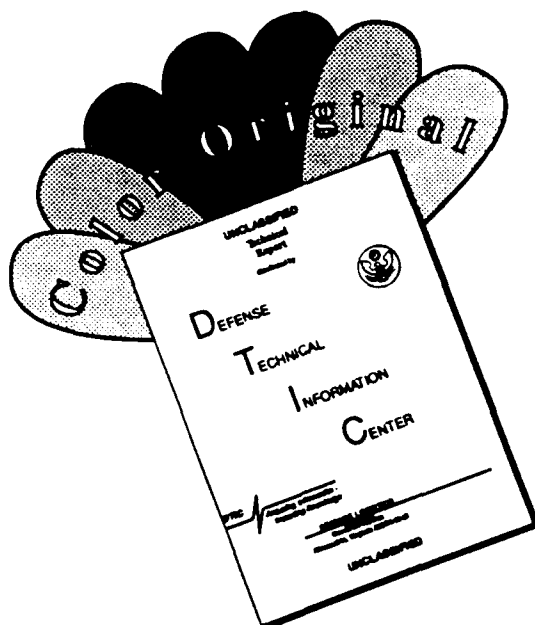
- A diagnostic analysis and code which can be used to help design turbine blades with increased efficiency and reduced cooling requirements.
- An open literature demonstration on the use of Computational Simulation and Scientific Visualization for gaining insight into complex turbomachinery flows.
- Acceleration of the transition of large-scale computational analyses to the turbomachinery design process through joint involvement between UTRC and Pratt and Whitney turbine engineers.
- A useful and proven analytical tool that can be used with existing and future engine design procedures.

The specific tasks associated with this effort are:



DISSEMINATION STATEMENT A
Approved for public release
Distribution Unlimited

DISCLAIMER NOTICE



THIS DOCUMENT IS BEST QUALITY AVAILABLE. THE COPY FURNISHED TO DTIC CONTAINED A SIGNIFICANT NUMBER OF COLOR PAGES WHICH DO NOT REPRODUCE LEGIBLY ON BLACK AND WHITE MICROFICHE.

- The ROTOR3 analysis will be extended by incorporating a three-dimensional hot streak at the stator inlet to numerically simulate the flow which exits a combustor. The effects of the combustor hot streak on turbine stator and rotor passage flows and blade surface heat transfer characteristics will be investigated. In addition, the ROTOR3 code will be extended to include a film cooling model in an effort to understand the effects of film cooling on stator and rotor blade surface heat transfer and on the flow through the downstream rotor. Both the hot streak and heat transfer investigations will be validated against data obtained from the UTRC Large Scale Rotating Rig (LSRR) experiments.
- The UTRC Scientific Visualization Laboratory will provide a means of exhibiting the important flow features. Advanced graphical representations are essential for reducing the massive amounts of numerical data that result from a calculation of three-dimensional viscous flows through multi-blade row turbomachinery passages. Scientific Visualization will be used to display details of the hot streak and film cooling flow paths as well as to provide information on blade surface heat transfer and mainstream flow temperature. The UTRC Scientific Visualization Lab will provide animated recordings for use by the Navy and others.

Quarterly Technical Progress Summary

Task I: Modify Code Boundary Conditions

No work was planned for Task I during this quarter

Task II: Verify and Improve Code

Two technical papers were presented at meetings during the past quarter which encompass work completed under Tasks II and III. The first technical paper, entitled "Navier-Stokes Analysis of Turbine Blade Heat Transfer and Performance," was presented at the *AGARD Symposium on CFD Techniques for Propulsion Applications* in San Antonio, Texas during the week of May 27. The objective of this paper was to establish the grid density requirements for accurately predicting blade surface and endwall heat transfer in a turbine passage. Simulations of transitional flow through the Langston cascade [3, 4] with a thin inlet boundary layer and heat transfer were performed. It was determined that for this particular geometry approximately 900,000 computational grid points are required to produce nearly grid-independent flow solutions. In addition, the study showed that overall aerodynamic turbomachinery blade row performance can be predicted within 2% using fine computational grids and the Baldwin-Lomax algebraic turbulence model. The second technical paper, entitled "Two-Dimensional Inlet Temperature Profile Attenuation in a Turbine Stage," was presented at the *36th ASME International Gas Turbine and Aeroengine Congress and Exposition* in Orlando, Florida, during the week of June 3. The purpose of this paper, which



AD-A235420

Availability Codes	
Dist	Avail and/or Special
A-1	

was prepared under a parallel Corporate Sponsored Research Program, was to determine if a two-dimensional Navier-Stokes procedure could be used to predict unsteady viscous flow through a 1-stator/1-rotor configuration with a *planar* hot streak introduced at the stator inlet. Using a new method for correlating the predicted results with the experimental data, the computational procedure accurately predicted the rotor airfoil pressure surface heating due to the hot streak. This investigation also demonstrated the importance of hot streak shape on the predicted results. In this investigation, the predicted results obtained with a two-dimensional Navier-Stokes procedure were compared with experimental data for a planar (i.e. two-dimensional) hot streak, whereas in previous two-dimensional numerical hot streak simulations the computational results were compared with experimental data obtained for a circular (i.e. fully three-dimensional) hot streak. Thus, for certain hot streak shapes, two-dimensional numerical simulations can be used in place of more expensive three-dimensional numerical simulations, giving designers an accurate and efficient tool for optimizing cooling systems. The papers are attached to this progress report as they are related to work completed to date under Tasks II and III.

Task III: Perform Numerical Experiments

The following numerical experiment is being performed using the ROTOR3 code:

- A 1-stator/1-rotor hot streak simulation with film cooling and heat transfer has been partially completed. In this investigation, the number and location of the film cooling slots has been varied to obtain both the qualitative and quantitative characteristics of the effectiveness of different film cooling schemes.

The computational grid topology used in the three-dimensional numerical simulation is similar to those used in a previous simulation [5]. The stator grid system is constructed with 101×21 grid points in each spanwise O-grid and 58×31 grid points in each spanwise H-grid. The rotor grid system is constructed with 101×21 grid points in each spanwise O-grid and 60×31 grid points in each spanwise H-grid. A total of 51 O-H grid planes are distributed in the spanwise direction. The rotor region has a tip clearance grid system that contains 101×11 grid points in each of 7 spanwise locations. A total of 410,677 grid points are used in the three-dimensional simulation. A wall spacing of 1.27×10^{-5} meters ($y^+ \approx 4$) is used in the blade-to-blade direction, while a wall spacing of 7.62×10^{-4} meters ($y^+ \approx 18$) is used in the spanwise direction.

In the first portion of the simulation, a heat flux was applied to the rotor surface *without* film cooling. The heat flux was specified to yield a surface temperature approximately 3-4 degrees less than the local adiabatic surface temperature. Figure 1 illustrates the rotor surface mid-span time-averaged temperature coefficient distributions for the adiabatic simulation [5] and the simulation with rotor surface heat transfer, where the time-averaged

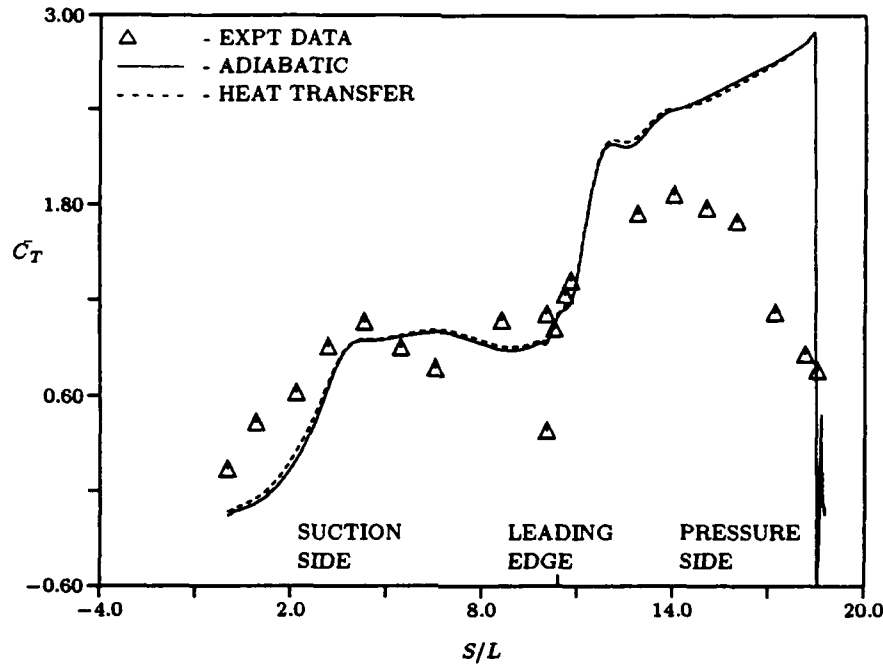


Figure 1: Rotor surface mid-span time-averaged temperature distributions with and without heat transfer

temperature coefficient is defined as:

$$\bar{C}_T = \frac{T - T_1}{T_{avg_{rle}} - T_1} \quad (1)$$

and T_1 is the free stream temperature outside the influence of the hot streak, T is the local time-averaged surface temperature, and $T_{avg_{rle}}$ is the time-averaged surface temperature at the rotor mid-span leading edge. The addition of a heat flux is seen to have little effect on the time-averaged rotor surface temperature distribution. This is expected considering the relatively small specified heat flux and the high local time-averaged surface temperatures due to the hot streak. A more negative heat flux value may reduce the influence of the hot streak on the surface temperature, but may also have adverse effects on the stability of the computational procedure. Figure 2 shows time-averaged temperature contours for the rotor pressure surface with heat transfer. The time-averaged temperature contours for this case are nearly identical to those obtained from the adiabatic hot streak simulation.

In the second portion of the simulation, fluid was injected through holes in the rotor pressure surface at a velocity equal to 0.2 times that of the free stream velocity and at an angle of 25 degrees with respect to the local axial direction surface tangent. The temperature of the injected fluid was specified to be 520° Rankine (2% lower than the free stream and 22%

TIME-AVERAGED TEMPERATURE CONTOURS
PRESSURE SURFACE

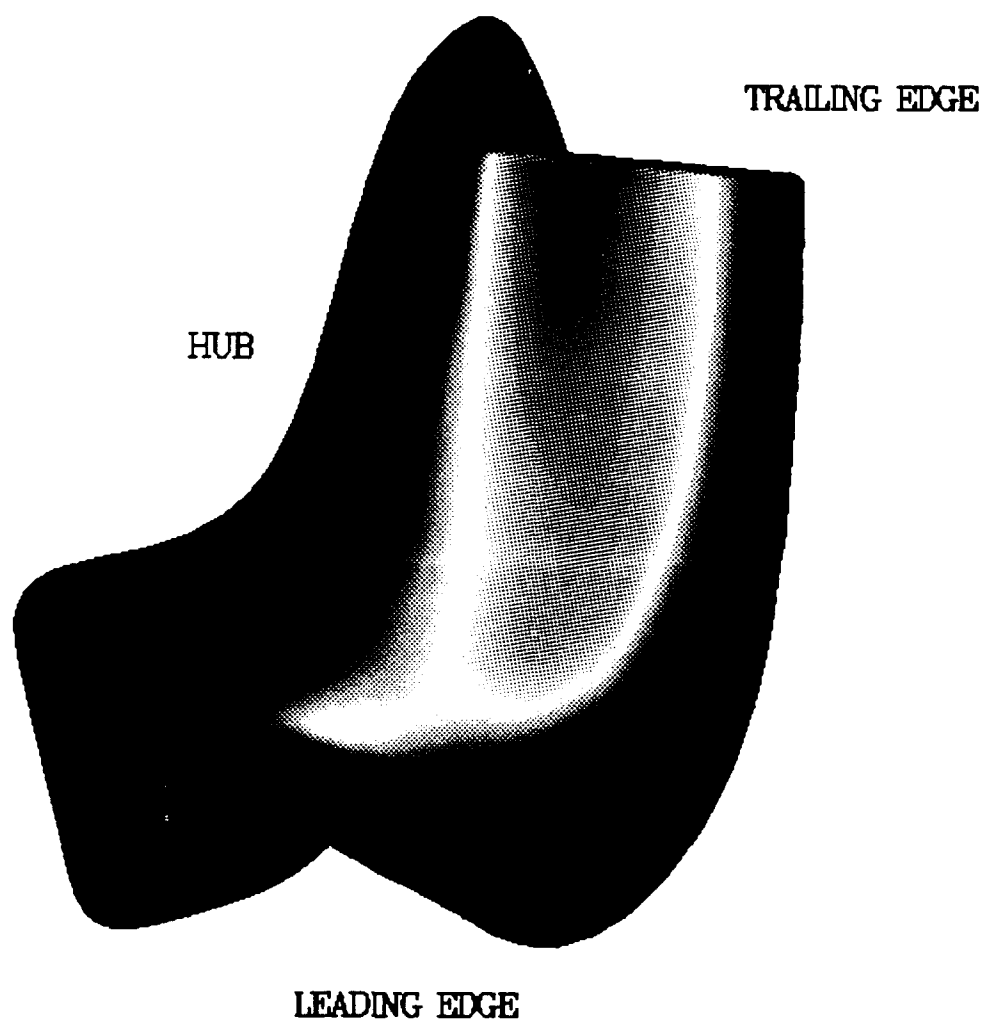


Figure 2: Time-averaged temperature contours for rotor pressure surface with heat transfer

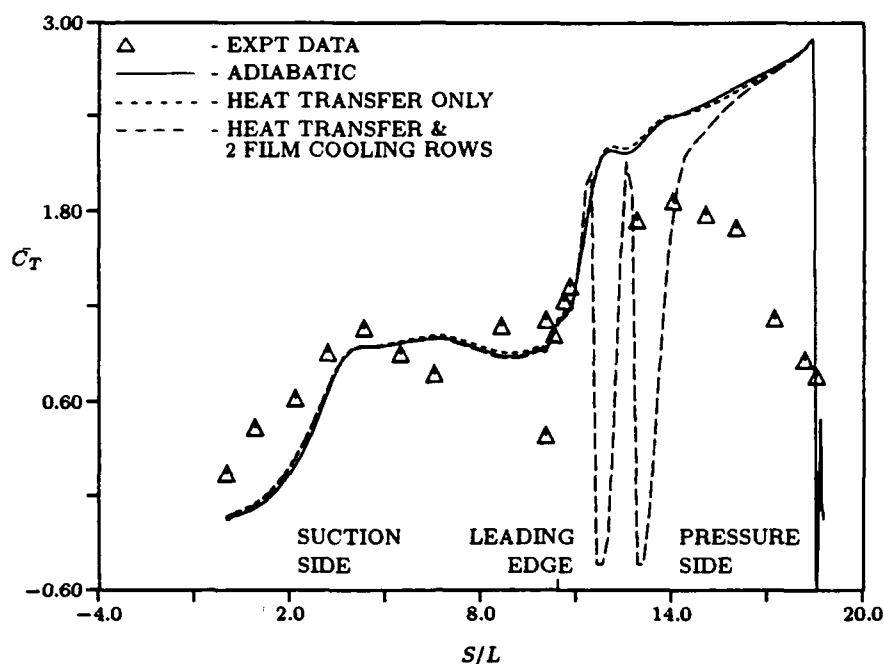


Figure 3: Rotor surface mid-span time-averaged temperature distributions for the adiabatic, heat transfer only, and two row film cooling/heat transfer simulations

lower than the hot streak) and the density ratio was chosen such that the static pressures at the injection locations were equal to the time-averaged static pressures in the absence of film cooling. The injection holes (ports) were located at 20% and 40% of the axial chord and extended from 20% of the span to 80% of the span at approximately 5% spanwise intervals. Similar to previous two-dimensional simulations [6], two-adjacent grid points were used to model an injection hole. A total of 22 injection holes were used in the first portion of the simulation. The surface heat flux was again specified to yield a surface temperature approximately 3-4 degrees less than the local adiabatic surface temperature.

Figure 3 illustrates the rotor surface mid-span time-averaged temperature coefficient distributions for the adiabatic simulation, the simulation with rotor surface heat transfer only, and the simulation with two film cooling rows and heat transfer. A substantial reduction of the time-averaged temperature on the rotor pressure surface is observed in the vicinity of the film cooling injection holes. As the cooling fluid convects downstream and away from the airfoil surface, the time-averaged surface temperature increases due to the influence of the hot streak. In this three-dimensional simulation, the time-averaged surface temperature in the region between film cooling injection holes and downstream of the last film cooling hole is seen to increase much more rapidly than that observed in similar two-dimensional simulations [6]. This may be partially due to the interaction between the

secondary and wall layer flows in the rotor passage, which cause the cooler injected fluid to mix very rapidly with the hot streak fluid. Another cause of the temperature increase may be that the current injection angle (25 degrees) is greater than that used in the two-dimensional simulations (10 degrees). While it appears to be beneficial to reduce the injection angle, realistically structural and manufacturing considerations would limit the actual range of possible injection angles. The current injection angle was chosen to be commensurate with those found in actual gas turbines. In spite of placing film cooling injection holes at 20% and 40% axial chord locations, the rapid mixing between the cooling fluid and the hot streak causes an increase in the temperature of the pressure surface near the trailing edge region. The time-averaged temperature on the rotor suction surface is unaffected since the film cooling holes were placed only on the pressure surface.

Figure 4 shows time-averaged temperature contours for the rotor pressure surface with 2 rows of film cooling holes and heat transfer. The film cooling locations are characterized by the dark blue (low temperature) contours. While discrete film cooling jets can be seen inboard of approximately 35% span and outboard of about 65% span, the cooling fluid near mid-span appears to be contained in one continuous jet. As noted above, the film cooling injection holes were spaced approximately every 5% of the span. In the mid-span region, the computational grid lines were also spaced approximately 5% of the span apart, resulting in 6 film cooling holes being placed at six consecutive grid points. Figure 4 shows that the combination of cooling fluid injection angle and secondary/boundary layer flow causes rapid mixing of the cooling fluid and allows the hot streak to increase the rotor pressure surface temperature aft of mid-chord region.

In an effort to eliminate the high time-averaged temperatures aft of mid-chord, a third row of film cooling holes was added at approximately 60% axial chord. Thus, in this portion of the simulation a total of 33 film cooling holes (each consisting of two adjacent grid points) were used. In addition, the injection velocity was increased to 0.4 times that of the free stream velocity. Figure 5 illustrates the rotor surface mid-span time-averaged temperature coefficient distributions for the adiabatic simulation, the simulation with rotor surface heat transfer only, and the simulation with three film cooling rows and heat transfer. In this simulation, the combination of a greater injection velocity and a third row of film cooling injection holes has effectively eliminated most of the high temperature regions on the rotor pressure surface. The high temperature region aft of mid-chord has been reduced, as has the high temperature regions between the film cooling injection holes. A small spike in the time-averaged temperature distribution is noticeable just upstream of the first row of film cooling holes and just downstream of the first and second rows of film cooling holes. These spikes may be due to the sudden change from a no-slip to a transpiration boundary condition, resulting in sudden changes in the density and velocity. The magnitude of these spikes increase as the film cooling velocity is increased, thus creating larger gradients in the flow variables. One possible technique for avoiding spikes is to gradually increase and decrease the film cooling parameters of adjacent computational nodes.

TIME-AVERAGED TEMPERATURE CONTOURS
PRESSURE SURFACE

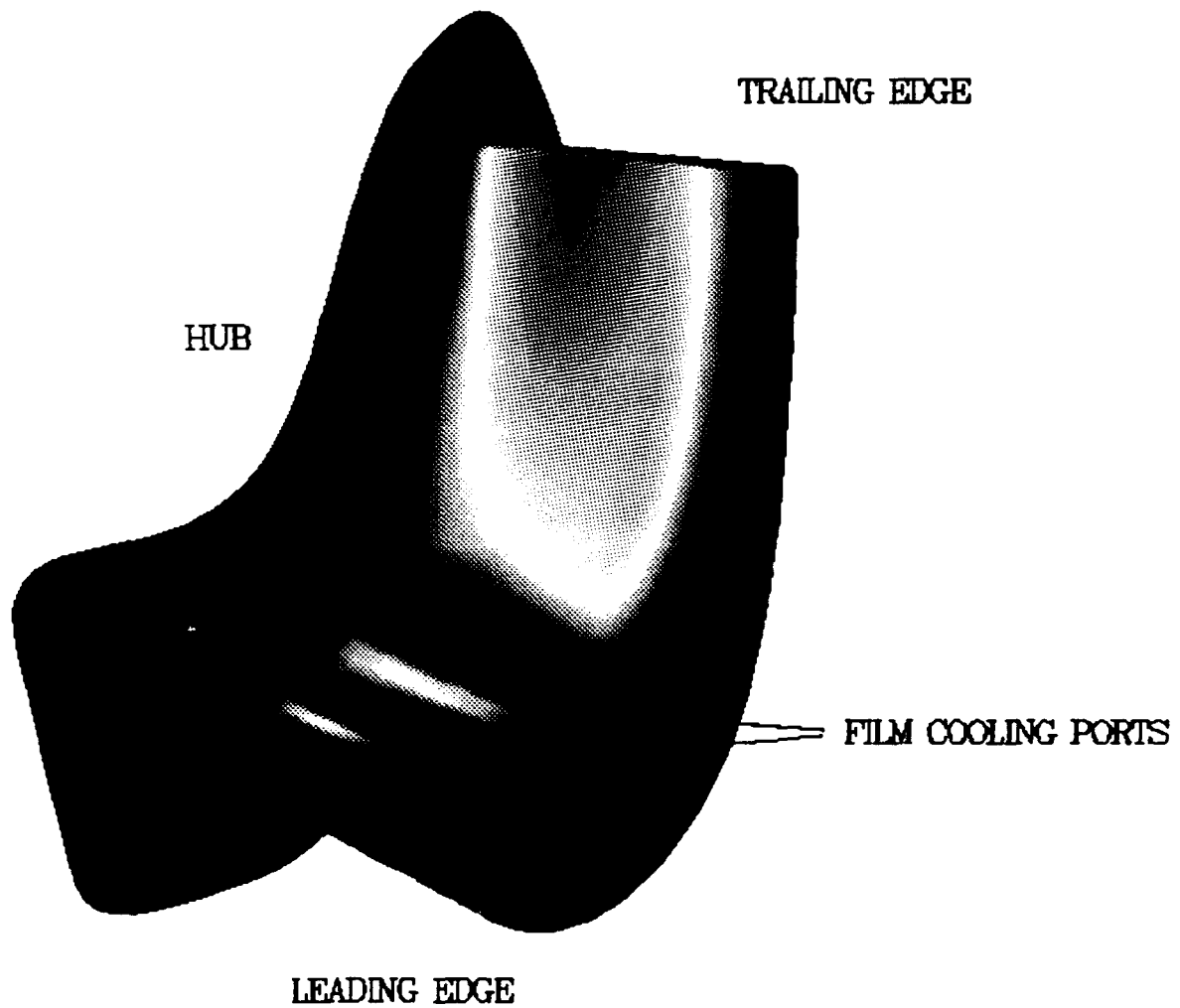


Figure 4: Time-averaged temperature contours for rotor pressure surface with two rows of film cooling holes and heat transfer

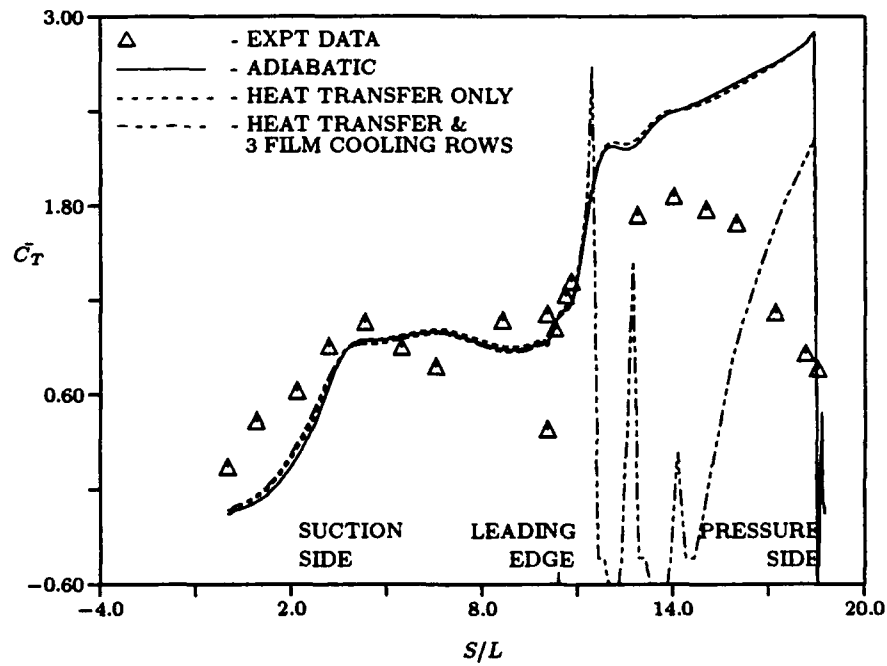


Figure 5: Rotor surface mid-span time-averaged temperature distributions for the adiabatic, heat transfer only, and 3 row film cooling/heat transfer simulations

Figure 6 shows time-averaged temperature contours for the rotor pressure surface with 3 rows of film cooling holes and heat transfer. The film cooling locations are again characterized by the dark blue (low temperature) contours. Comparing Figs. 4 and 6 shows that increasing the injection velocity extends the range of effectiveness of the cooling fluid. Figure 6 also illustrates that the addition of a third row of film cooling holes has significantly decreased the time-averaged rotor pressure surface temperature aft of the mid-chord point. A fourth row of film cooling holes placed at approximately 80% chord would probably eliminate the lingering remnants of the hot streak in the trailing edge region.

Task IV: Utilize Scientific Visualization

A video animation of the predicted results from a two-dimensional 3-stator/4-rotor/1-hot streak simulation with film cooling and heat transfer was created. The video, which illustrated static temperature contours, was constructed using 80 time segments obtained during one passing cycle of the rotor. The video was used to study the migration of the cooling fluid, which was injected from the trailing edge of the stators and from the pressure surface of the rotors.

Work Planned

Task I: Modify Code Boundary Conditions

No work is planned for Task I.

Task II: Verify and Improve Code

No work is planned for Task II.

Task III: Perform Numerical Experiments

The three-dimensional 1-stator/1-rotor/1-hot streak simulations with film cooling and heat transfer will be completed and the predicted unsteady and time-averaged flow fields will be analyzed in greater detail.

Task IV: Utilize Scientific Visualization

Work will be initiated on visualizing and animating the predicted flow field for the three-dimensional hot streak simulation including the effects of film cooling and heat transfer.

TIME-AVERAGED TEMPERATURE CONTOURS
PRESSURE SURFACE

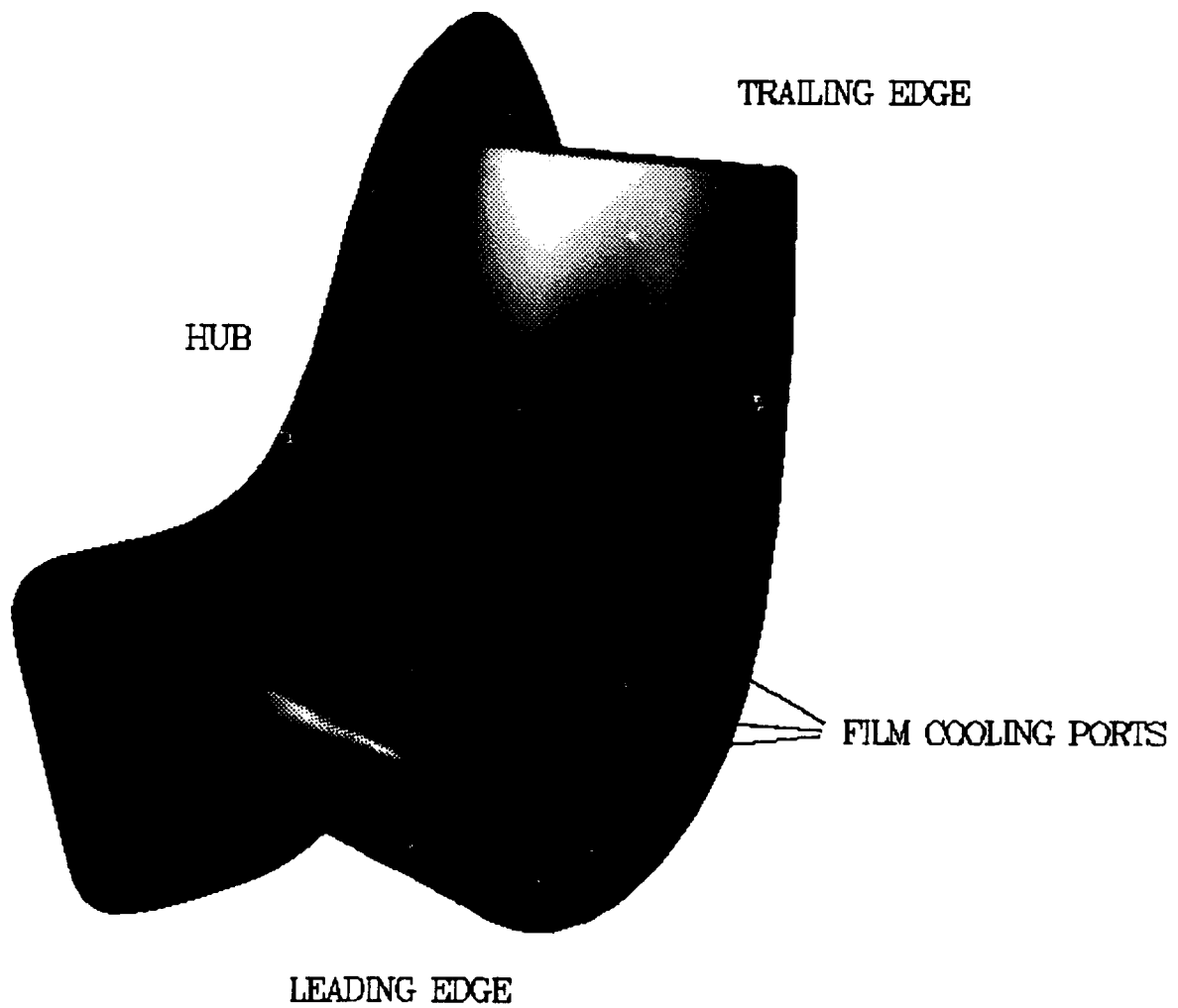


Figure 6: Time-averaged temperature contours for rotor pressure surface with three rows of film cooling holes and heat transfer

Task IV: Reporting

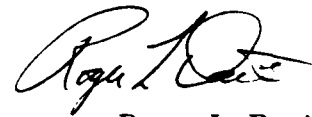
Work on the final technical report will be initiated.

References

- [1] Rai, M. M., "Unsteady Three-Dimensional Navier-Stokes Simulations of Turbine Rotor-Stator Interaction" AIAA Paper No. 87-2058, 1987.
- [2] Rai, M. M. and Dring, R. P., "Navier-Stokes Analyses of the Redistribution of Inlet Temperature Distortions in a Turbine," AIAA Paper 87-2146, 1987.
- [3] Langston, L. S., Nice, M. L., and Hooper, R. M., "Three-Dimensional Flow Within a Turbine Cascade Passage," ASME Paper No. 76-GT-50, March, 1976.
- [4] Graziani, R. A., Blair, M. F., Taylor, J. R., and Mayle, R. E., "An Experimental Study of Endwall and Airfoil Surface Heat Transfer in a Large Scale Turbine Blade Cascade," *Journal of Engineering for Power*, Vol. 102, No. 2, April, 1980, pp.257-267.
- [5] Dorney, D. J., Davis, R. L., Edwards, D. E., and Madavan, N. K., "Unsteady Analysis of Hot Streak Migration in a Turbine Stage," AIAA Paper 90-2354, also accepted for publication in the *Journal of Propulsion and Power*, 1990.
- [6] Dorney, D. J. and Davis, R. L., "Investigation of Hot Streak Migration and Film Cooling Effects on the Heat Transfer in Rotor/Stator Interacting Flows", Quarterly Progress Report R91-957927-1, March 31, 1991.



Daniel J. Dorney
Associate Research Engineer



Roger L. Davis
Senior Research Engineer

Two-Dimensional Inlet Temperature Profile Attenuation in a Turbine Stage

Daniel J. Dorney and Roger L. Davis
Theoretical & Computational Fluid Dynamics Group
United Technologies Research Center
East Hartford, CT 06108
and
Om P. Sharma
Turbine Group
Pratt & Whitney
East Hartford, CT 06108

ABSTRACT

Experimental evidence has shown that hot streaks which are emitted from the combustors of gas turbines are often largely responsible for the burning of first stage turbine blades. Designers have attempted to counteract the effects of these hot streaks through the use of complex internal and film cooling schemes. Unfortunately, due to the lack of accurate predictive tools which account for temperature non-uniformities in the gas path, as well as a lack of detailed understanding of the physical mechanisms which control the migration and accumulation of the hot streak gases, turbine blade "hot spots" still occasionally occur. In an effort to increase understanding of the interaction mechanisms between combustor hot streaks and turbine blade heat transfer, a numerical investigation has been conducted to determine if a two-dimensional solution procedure can accurately predict rotor airfoil surface heating for flows which include planar hot streaks. A two-dimensional Navier-Stokes analysis is used to predict unsteady viscous flow through a 1-stator/1-rotor configuration with a planar hot streak introduced at the stator inlet. Comparison of the predicted results with a new experimental data set demonstrates that the two-dimensional numerical procedure can be used to accurately predict time-averaged rotor pressure surface temperatures for flows which include planar hot streaks.

Nomenclature

a	- Speed of sound
e	- Specific energy
e_t	- Total energy
J	- Jacobian of transformation
M	- Mach number
P	- Static pressure
Pr	- Prandtl number
R	- Universal gas constant

Re	- Free stream inlet reference Reynolds number
T	- Static temperature
u, v	- x, y components of velocity
U	- Rotor velocity
β	- Rotor inlet relative flow angle
κ	- Thermal conductivity
μ, λ	- First and second coefficients of viscosity
ρ	- Density
τ	- Shear stress

Subscripts

c	- Cold flow
HS	- Hot streak
i	- Inviscid
L	- Laminar quantity
t	- Stagnation quantity
T	- Turbulent quantity
v	- Viscous
w	- Wall value
x, y	- First derivative with respect to x or y
xx, yy	- Second derivative with respect to x, y
1	- Inlet quantity
2	- Exit quantity

INTRODUCTION

In recent years, design engineers have achieved substantial increases in turbine stage efficiencies by increasing combustor operating temperatures. The increased temperature of the combustor exit flow has necessitated the implementation of complex cooling schemes to avert burning of first stage turbine airfoils. In an effort to optimize the various cooling schemes, engineers have simulated (both experimentally (Butler *et al.* 1989) and compu-

tationally (Krouthen and Giles, 1988, Dorney *et al*, 1990, Takahashi and Ni, 1990, Sharma *et al*, 1990, Rai and Dring, 1990)) the "hot streaks" which exit the combustor and migrate through the turbine stage. The goal of these simulations has been to isolate the various factors associated with combustor hot streaks which lead to excessive temperatures and burning of first stage turbine blade pressure surfaces.

The work of Butler *et al* (1989) represents a detailed experimental investigation of hot streak migration. In this experiment, a three-dimensional hot streak was introduced into the stator inlet of a turbine stage through a circular pipe. The hot streak was seeded with CO_2 , and the path of the hot streak was tracked by sampling the CO_2 concentrations at various locations in the turbine stage. According to Butler *et al* (1989), the experimental simulations indicate that hot streak migration paths and rotor surface heating are controlled by a) the secondary flows in the rotor passage, and b) the segregation of hot and cold gases caused by the difference in the rotor inlet flow angle between the hot and cold gases.

Attempts to reproduce the circular hot streak experimental results of Butler *et al* (1989) using two-dimensional computational techniques have only been partially successful (Krouthen and Giles, 1988, Dorney *et al*, 1990, Rai and Dring, 1990). The discrepancies between the predicted two-dimensional results and experimental data are probably due to a combination of factors, including a) the effects of secondary and endwall flows, b) the three-dimensional shape of this particular experimental hot streak, c) the assumed correlation between CO_2 (used in the experiments to track the movement of the hot streak) and temperature, d) the hot streak to rotor passage count, and e) the ratio of the hot streak temperature to that of the surrounding flow.

Some progress has been made in isolating the role of three-dimensional and viscous effects on hot streak migration (Dorney *et al*, 1990, Takahashi and Ni, 1990, Sharma *et al*, 1990) and turbine rotor heat transfer. Both a three-dimensional Navier-Stokes (Dorney *et al*, 1990) and an Euler simulation (Takahashi and Ni, 1990, Sharma *et al*, 1990) in which viscous effects were modelled have demonstrated better agreement with the circular hot streak experimental data (Butler *et al*, 1989) than previous two-dimensional simulations for the time-averaged temperature on the rotor pressure surface.

The goal of the current research effort is to determine if two-dimensional unsteady rotor/stator/hot streak simulations can provide reliable warnings as to when rotor surface temperatures become too high due to combustor hot streaks. If two-dimensional simulations can be shown to be useful in providing this guidance, then the need to execute costly and time-consuming three-dimensional simulations can be reduced or eliminated. Computational results for a two-dimensional hot streak simulation are compared with new experimental data for a two-dimensional planar hot streak which was introduced across the span of a turbine stage stator inlet. An important mechanism which has been identified as a controlling factor on the surface temperature of turbine

rotors is hot streak shape. By understanding the strengths and limitations of two-dimensional hot streak simulations, useful insights can be obtained which will improve turbine blade designs.

Results of a 1-stator/1-rotor hot streak migration simulation of the Large Scale Rotating Rig (LSRR) (Butler *et al*, 1989) are compared with experimental data recently obtained for a planar hot streak. The close agreement between the numerical results and the experimental data suggests that two-dimensional numerical analyses can be used to accurately predict rotor pressure surface temperature distributions.

NUMERICAL INTEGRATION PROCEDURE

The governing equations of motion considered in this study are the time dependent two-dimensional Navier-Stokes equations, which can be written in Cartesian coordinates as:

$$U_t + (F_i + F_v)_x + (G_i + G_v)_y = 0 \quad (1)$$

where

$$U = \begin{bmatrix} \rho \\ \rho u \\ \rho v \\ e_t \end{bmatrix} \quad (2)$$

$$F_i = \begin{bmatrix} \rho u \\ \rho u^2 + P \\ \rho uv \\ (e_t + P)u \end{bmatrix} \quad F_v = - \begin{bmatrix} 0 \\ \tau_{xx} \\ \tau_{xy} \\ \tau_{hx} \end{bmatrix} \quad (3)$$

$$G_i = \begin{bmatrix} \rho v \\ \rho uv \\ \rho v^2 + P \\ (e_t + P)v \end{bmatrix} \quad G_v = - \begin{bmatrix} 0 \\ \tau_{yx} \\ \tau_{yy} \\ \tau_{hy} \end{bmatrix} \quad (4)$$

where

$$\begin{aligned} \tau_{xx} &= 2\mu u_x + \lambda(u_x + v_y) \\ \tau_{xy} &= \mu(u_y + v_x) \\ \tau_{yx} &= \tau_{xy} \\ \tau_{yy} &= 2\mu v_y + \lambda(u_x + v_y) \\ \tau_{hx} &= u\tau_{xx} + v\tau_{xy} + \gamma\mu P_r^{-1}e_x \\ \tau_{hy} &= u\tau_{xy} + v\tau_{yy} + \gamma\mu P_r^{-1}e_y \\ e &= \frac{P}{(\rho(\gamma - 1))} \\ e_t &= \rho e + \frac{\rho(u^2 + v^2)}{2} \end{aligned}$$

For the present application, the second coefficient of viscosity is calculated using Stokes' hypothesis, $\lambda = -2/3\mu$. The equations of motion are completed by the perfect gas law.

The viscous fluxes can be simplified by incorporating the thin layer assumption (Baldwin and Lomax, 1978). The thin layer

assumption states that for high Reynolds number flows, the diffusion terms normal to a solid surface will be much greater than those parallel to the surface. In the current study, viscous terms are retained in the direction normal to the blade surface.

To extend the equations of motion to turbulent flows, an eddy viscosity formulation is used. Thus, the effective viscosity and effective thermal conductivity can be defined as:

$$\begin{aligned} \mu &= \mu_L + \mu_T \\ \frac{\kappa}{C_p} &= \frac{\mu_L}{Pr_L} + \frac{\mu_T}{Pr_T} \end{aligned} \quad (5)$$

The turbulent viscosity, μ_T , is calculated using the two-layer Baldwin and Lomax (1978) algebraic turbulence model.

The numerical procedure for the two-dimensional analysis consists of a time marching, implicit, third-order spatially accurate, upwind, finite difference scheme. The inviscid fluxes are discretized according to the scheme developed by Osher (Chakravarthy and Osher, 1982). The viscous fluxes are calculated using standard central differences. An alternate direction, approximate-factorization technique is used to compute the time rate changes in the primary variables. In addition, an inner Newton iteration is used to increase stability and reduce linearization errors.

GRID GENERATION

The current two-dimensional Navier-Stokes analysis uses multiple zonal grids to discretize the rotor/stator flow field and facilitate relative motion of the rotor (Rai *et al.*, 1988,1989). A combination of O- and H-grid sections are generated in the blade-to-blade direction extending upstream of the stator leading edge to downstream of the rotor trailing edge. Algebraically generated H-grids are used in the regions upstream of the leading edge, downstream of the trailing edge and in the inter-blade region. The O-grids, which are body-fitted to the surfaces of the airfoils and generated using an elliptic equation solution procedure, are used to properly resolve the viscous flow in the blade passages and to easily apply the algebraic turbulence model. Computational

grid lines within the O-grids are stretched in the blade-normal direction with a fine grid spacing at the wall. Figure 1 illustrates the grid topology used in the current simulations.

BOUNDARY CONDITIONS

The theory of characteristics is used to determine the boundary conditions at the stator inlet and rotor exit. For subsonic inlet flow, the total pressure, tangential velocity component and the downstream running Riemann invariant, $R_1 = u + \frac{2a}{\gamma-1}$, are specified while the upstream running Riemann invariant, $R_2 = u - \frac{2a}{\gamma-1}$, is extrapolated from the interior of the computational domain. Inlet flow boundary conditions within the hot streak region are updated using Riemann invariants where the velocity and speed of sound reflect the static and stagnation temperature increase in the hot streak. The static and total pressure in the hot streak are assumed to be equal to that of the undisturbed inlet flow, corresponding to the experimental conditions. For subsonic outflow the pressure is specified while the tangential component of velocity, entropy, and the downstream running Riemann invariant are extrapolated from the interior of the computational domain. Absolute no-slip boundary conditions are enforced on stator airfoil surfaces, while relative no-slip boundary conditions are imposed along the rotor airfoil surfaces. Periodicity is enforced along the outer boundaries of the H-grids in the circumferential (y) direction. In the present, study the flow is assumed to be adiabatic.

Dirichlet conditions, in which the time rate change in the vector U of Eq. (2) is set to zero, are imposed at the patched boundaries of the O- and H-grids in the stator and rotor regions. The flow variables of U at the zonal boundaries are explicitly updated after each time step by interpolating values from the adjacent grid. Because of the explicit application of the zonal boundary conditions, large time steps necessitate the use of more than one Newton iteration. The zonal boundary conditions are non-conservative, but for subsonic flow this should not affect the accuracy of the final flow solution. Further information describing the implementation of the boundary conditions can be found in Rai *et al.* (1985,1988,1989,1990).

RESULTS

A numerical investigation of hot streak migration has been conducted in which the predicted results from a two-dimensional Navier-Stokes procedure have been compared with experimental data. The turbine airfoil geometry used in this study consisted of the first stage of the UTRC Large Scale Rotating Rig (LSRR) (Dring *et al.*, 1982, Butler *et al.*, 1989) which includes 22 stator airfoils and 28 rotor airfoils. An accurate simulation of this configuration would require at least 11 stator airfoils and 14 rotor airfoils. For the current 1-stator/1-rotor simulation, a rescaling strategy was used to reduce the number of airfoils to 1 stator and 1 rotor. It was assumed that there were 28 stator airfoils and 28 rotor airfoils and the stator was scaled down by the factor (22/28). To replicate the test conditions of the experimental

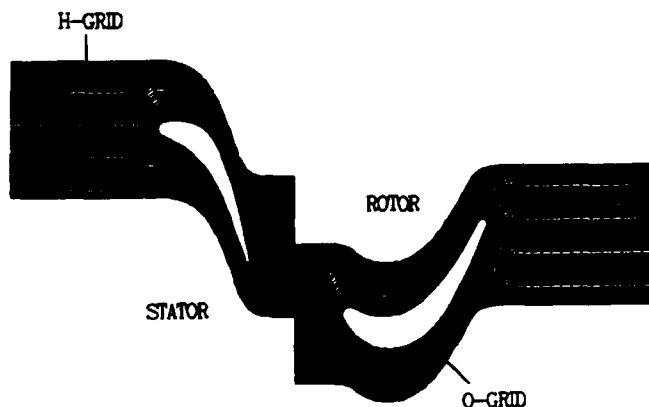


Figure 1: 2-D computational grid

study, a 65% axial gap was used between the stator and rotor airfoils. The numerical simulation was performed at the experimental stator inlet Mach number of $M = .051$. In both the experiment and the numerical simulation, the stator vanes were rotated down 7 degrees with respect to the tangential direction relative to the design point operating conditions. The experimental rotor rotation speed was 710 rpm. The Reynolds number in both the experiment and numerical simulation was 100,000 per inch and a pressure ratio of $P_2/P_{t1} = .9640$ was determined from the inlet total pressure and the static pressure measured in the trailing-edge plane.

In the experimental study, one hot streak was introduced in the form of a two-dimensional jet from the hub to the tip between two stator airfoils of the LSRR (i.e. one hot streak for the entire wheel). The temperature of the hot streak was twice that of the surrounding inlet flow, whereas the hot streak static and stagnation pressures were identical to the free stream. The hot streak was seeded with CO_2 and the path of the hot streak determined by measuring CO_2 concentrations at various locations within the turbine stage using the blade surface static pressure taps. In the numerical simulation, one hot streak is introduced to the inlet of every stator passage in the form of a hyperbolic tangent (step-like) temperature profile. A hot streak temperature of 1.2 times that of the surrounding inlet flow was chosen for this investigation. Shear layer instabilities, caused by the step-like temperature profile, developed in the numerical simulations when the hot streak temperature was increased beyond 1.2 times that of the surrounding flow. The predicted temperature distributions of the current study can still be related to the experimental data using the temperature coefficient scaling technique developed by Sharma *et al* (1990). In the 1-stator/1-rotor simulation, the hot streak was introduced over one quarter of the stator pitch and centered at midgap.

For the 1-stator/1-rotor simulation, the stator grid system was constructed with 101×31 (streamwise \times tangential) grid points in the O-grid and 85×51 grid points in the H-grid. The rotor grid system was constructed with 101×31 grid points in the O-grid and 78×51 grid points in the H-grid. A total of 14,575 grid points were used in this simulation. The stator airfoils had an average y^+ value of 0.84, while the rotor airfoils had an average y^+ value of 0.70. Figure 1 illustrates the grid topology used in the numerical simulations, where every other grid point in the O-grid has been omitted for clarity.

The numerical simulations performed during this investigation were computed on a four processor Alliant FX-80 minisupercomputer. Typical calculations required .00191 seconds per grid point per iteration computation time. In the current study, approximately six cycles at 2000 iterations per global cycle were needed to obtain a time-periodic solution.

In the experiment, the flow coefficient was held at $\phi_c = u_c/U = .35$. The subscript 'c' refers to the fact that the flow coefficient is based on the inlet velocity in the regions outside the hot streak (i.e. cold flow). Within the hot streak, a velocity increase proportional to $\sqrt{T_{h0}/T_{\infty}}$ causes a significant increase

in the average flow coefficient, $\phi = u/U$. Thus, in the numerical simulation, where a hot streak is included in every passage, the effect of this velocity increase within the hot streak on the flow coefficient must be taken into account. In addition, previous experimental data (Dring *et al*, 1982) and numerical simulations indicate that at a flow coefficient of $\phi = .35$ the flow separates on the pressure surface of the rotor. To avoid the additional complications that flow separation may present in interpreting the numerical results, the flow coefficient in the numerical simulation was increased until the time-averaged pressure side separation disappeared (approximately $\phi_c = .385$). The difference in the flow coefficients equates to the numerical simulation being performed at approximately 5 degrees more positive incidence at the rotor inlet than in the experiment. This increase in incidence corresponds to only a 10% shift in the spanwise location (towards the tip) at which the numerical simulation was performed, to a position located at 60% span. At this low flow coefficient, a 50 deg variation in the incidence occurs from the hub to the tip of the rotor airfoil. This can be shown using an analytic expression which relates the rotor inlet relative flow angle to the flow coefficient (assuming a given blade geometry):

$$\cot \beta = \cot \alpha - \phi^{-1} \quad (6)$$

where α is the absolute flow angle at the stator exit. As Figure 2 illustrates, the rotor inlet flow angle changes very rapidly with flow coefficient for this particular geometry.

In order to understand the incidence variation at the rotor inlet caused by the hot streak and stator wakes, a study was performed to determine their relevance. By taking the derivative of eq. (6), an equation is obtained which relates the change in the rotor inlet relative flow angle to the change in the flow coefficient:

$$\Delta \beta = \Delta \phi / \csc^2 \beta \quad (7)$$

where β is the mean rotor relative inlet flow angle, $\Delta \phi$ is the variation in the flow coefficient due to a hot streak or stator wake, and $\Delta \beta$ is the change in the rotor inlet relative flow angle.

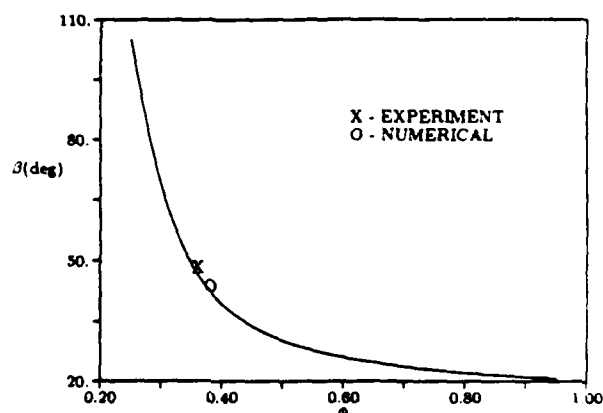


Figure 2: Rotor inlet relative flow angle vs flow coefficient

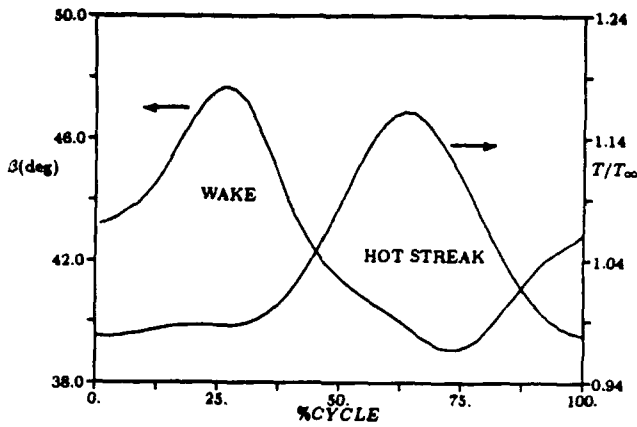


Figure 3: Rotor inlet flow angle and static temperature distributions

Equation (7) is useful in estimating the change in the rotor inlet relative flow angle as the rotor passes through the hot streak. For the present numerical simulation, eq. (7) predicts a 4.12 deg variation in the rotor inlet relative flow angle due to the hot streak. Figure 3 shows the numerically predicted rotor inlet relative flow angle and static temperature for one cycle, where a cycle corresponds to the rotor blade rotating through an angle of $2\pi/N$ where N is the number of stator blades (i.e. $N=28$ for the present simulations). The stator wake has little effect on the rotor inlet static temperature, but has a significant impact on the relative flow angle. The wake causes the rotor inlet relative flow angle to vary by approximately 4.9 deg in the direction of more negative incidence and affects the flow angle for nearly 50% of the cycle. The hot streak is seen to cause a variation in both the static temperature and relative inlet flow angle. The hot streak causes the rotor inlet relative flow angle to vary by approximately 3.9 deg (compared to 4.12 deg calculated above) in the direction of more positive incidence and affects the flow angle for about 50% of the cycle. Thus, through the course of one cycle the rotor inlet relative flow angle varies by almost 10 deg, although the incidence variation in the rotor caused by the stator wake is nearly cancelled by that corresponding to the hot streak for time-averaged flow. Figure 3 also shows that the flow angle variation due to the hot streak lags the temperature increase due to the hot streak.

Figure 4 illustrates the predicted stator surface time-averaged pressure coefficient distribution. Unfortunately, no experimental time-averaged pressure data was available for the stator airfoils. The time-averaged pressure coefficient is defined as:

$$C_p = \frac{2(P_{avg} - P_{t1})}{\rho_1 U^2} \quad (8)$$

where P_{avg} is the local time-averaged pressure, P_{t1} is the inlet total pressure, ρ_1 is the average inlet free stream density, and U is the rotor velocity. Figure 5 shows the predicted and experimental (Dring *et al*, 1982) rotor surface time-averaged pressure coefficient distributions. While the experimental data of Dring *et al* (1982) is for rotor/stator flow without a hot streak, past simulations (Dorney *et al*, 1990, Rai and Dring, 1990) have shown

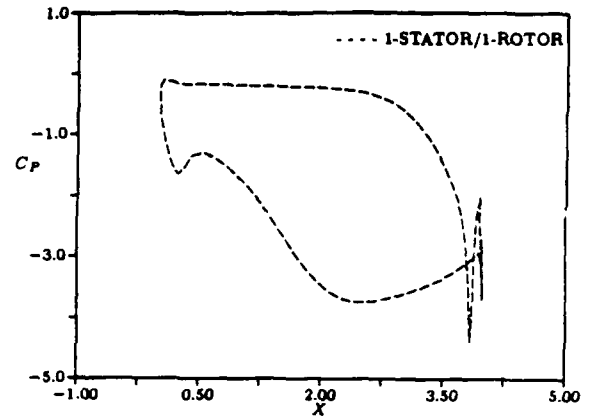


Figure 4: Predicted pressure coefficient distribution for the stator

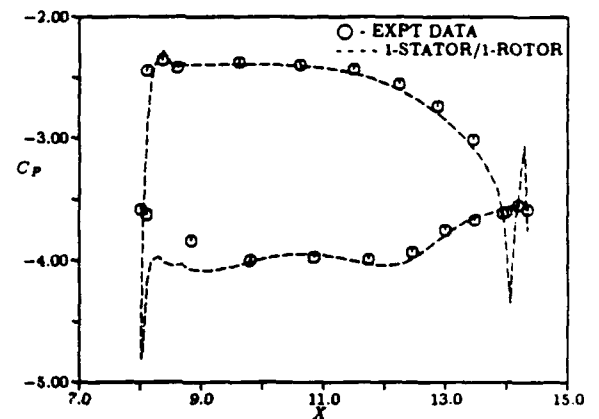


Figure 5: Predicted and experimental pressure coefficient distributions for the rotor

that for the present type of simulation, the pressure and temperature fields are decoupled. Excellent agreement exists between the predicted results and the experimental data for the rotor, except near the suction surface leading edge where the numerical simulation predicts a strong overspeed. This discrepancy is probably due to the slight difference (1 deg) in the time-averaged incidence to the rotor between the numerical simulation and the experiment (Dring *et al*, 1982).

The migration path of the numerical hot streak is displayed in Fig. 6, which shows static temperature contours at one instant in time during the course of a cycle. The hot streak is undisturbed as it migrates through the stator passage, except that the width of the hot streak decreases due to flow acceleration. The geometry of the rotor blade is such that the hot streak first impinges upon the pressure surface, then wraps around the leading edge and moves along the suction surface. The hot fluid on the suction surface is quickly convected downstream, while the hot fluid near the pressure surface remains in the rotor passage for some time after the rotor passes through the hot streak. The hot streak assumes a V shape (due to the difference in convection

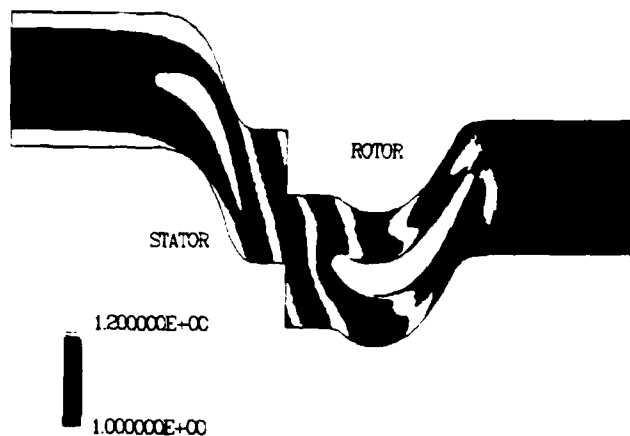


Figure 6: Static temperature contours for the LSRR turbine stage

speeds between the pressure and suction sides of the passage) as it continues to move downstream through the rotor passage, before breaking up and leaving the turbine in the form of discrete temperature eddies.

Figure 7 illustrates the experimental time-averaged CO_2 concentration contours for the rotor surface. The movement of the hot streak fluid from leading edge to the trailing edge of the pressure surface at approximately constant spanwise locations indicates the two-dimensional nature of the hot streak. Conspicuously absent is the radial migration of the hot streak on the pressure surface observed both experimentally (Butler *et al.* 1989) and in previous numerical simulations (Dorney *et al.* 1990, Takahashi and Ni, 1990) for a circular hot streak. Figure 8 compares the predicted time-averaged temperature coefficient distribution along the surface of the rotor to the experimental data taken at midspan. The temperature coefficient, \bar{C}_T , is defined as (Takahashi and Ni, 1990, Sharma *et al.* 1990):

$$\bar{C}_T = \frac{T - T_1}{T_{avg,le} - T_1} \quad (9)$$

where T is the local time-averaged temperature and $T_{avg,le}$ is the time-averaged temperature at the rotor leading edge. Results of the numerical simulation show fair agreement with the

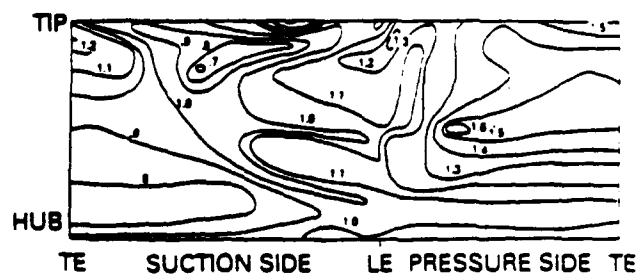


Figure 7: Experimental time-averaged CO_2 contours for the LSRR rotor

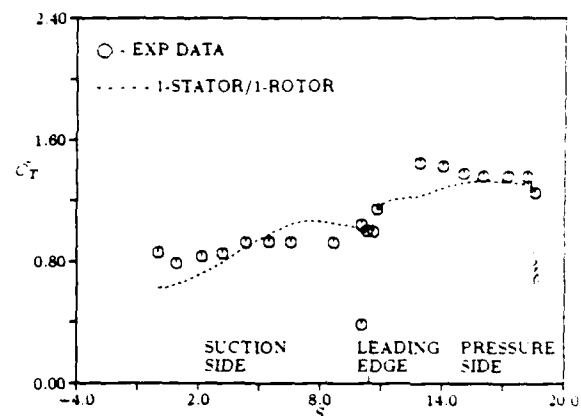


Figure 8: Predicted and experimental rotor surface temperatures - \bar{C}_T

planar hot streak experimental data. The numerical simulation underpredicts the temperature near the pressure surface leading edge, and also predicts a rapid temperature fall-off on the suction surface which is not observed in the experimental data. Figure 9 shows the time-averaged temperature contours for the entire rotor passage. The accumulation of hot streak fluid on the pressure side of the passage is evident. A close-up of the rotor pressure surface leading edge region (see Figure 10) shows that a region of cooler fluid is trapped between the hot streak fluid and the rotor surface. Similar results were reported in Dorney *et al.* (1990), for a two-dimensional hot streak simulation at different operating conditions. Figure 11, which shows time-averaged temperature profiles at three locations along the pressure surface of the rotor, also indicates the presence of a cooler region near the surface at the leading edge. Time-averaged boundary layer edge-

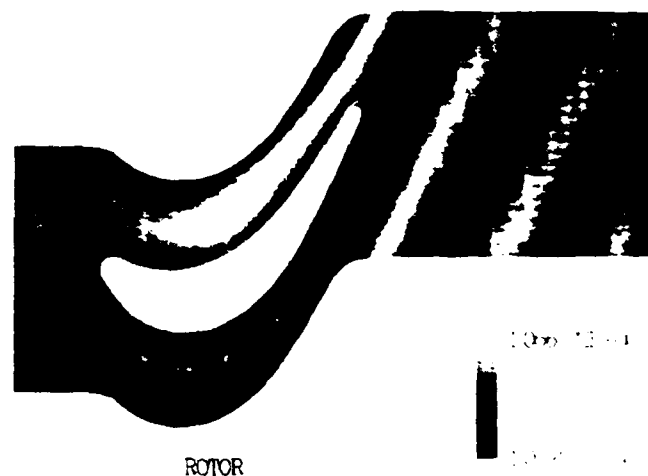


Figure 9: Time-averaged temperature contours for the rotor passage

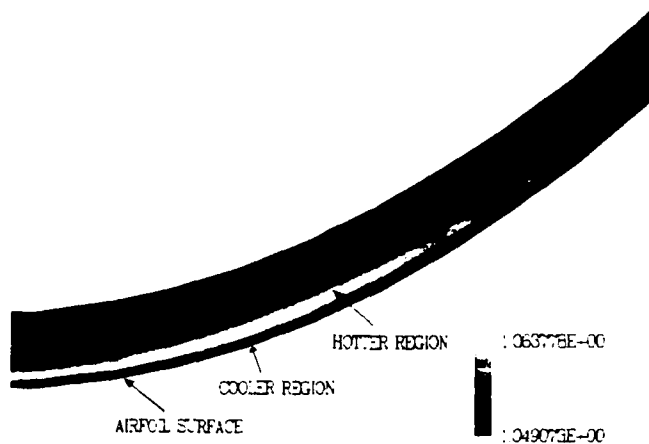


Figure 10: Time-averaged temperature contours near the rotor pressure surface leading edge

locations are also included in Figure 11. At 25% axial chord the maximum temperature in the boundary layer occurs off the surface, approximately one-third the distance to the boundary layer edge. Similarly, at 50% axial chord the maximum temperature occurs well above the rotor surface. At 75% axial chord, however, the time-averaged boundary layer is noticeably thinner and the maximum time-averaged temperature occurs at the rotor surface. A general observation drawn from this investigation is that as the boundary layer becomes thinner, the maximum temperature in a given boundary layer profile moves closer to the airfoil surface.

The differences between the experimental data and the predicted surface temperatures shown in Fig. 8 may be due to one of several factors. As shown in Dorney *et al* (1990), Takahashi and Ni (1990), and Sharma *et al* (1990) a significant effect on the surface temperature exists (for certain hot streak shapes) due to the three-dimensionality of the rotor surface boundary layers and the influence of secondary flows. A second factor which may also contribute to the discrepancies between the experimental data

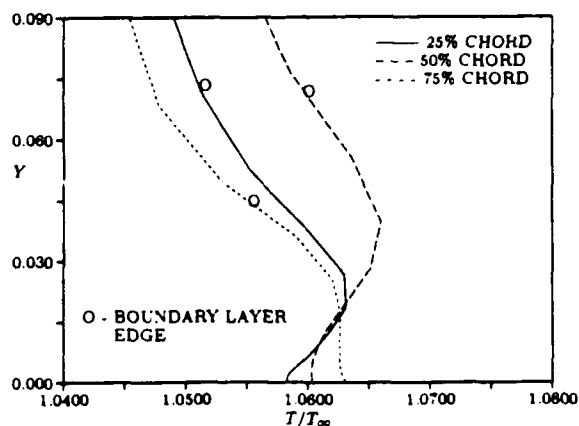


Figure 11: Predicted time-averaged temperature profiles

and the two-dimensional simulation is the assumed correlation between the predicted surface temperature and the experimentally measured CO_2 concentrations. In the experiment, the CO_2 concentrations along the surface of the rotor were determined by drawing samples of the gas in through static pressure taps. The suction force may cause CO_2 gas from well above the airfoil surface to be included in the sample. To test this hypothesis, the time-averaged temperature coefficient was redefined as:

$$C_T = \frac{T_{bl} - T_1}{T_{avg,ric} - T_1} \quad (10)$$

where T_{bl} is the time-averaged temperature, area-averaged over a given boundary layer profile. Figure 12 compares the predicted results using the modified temperature coefficient definition with the experimental data. Excellent agreement now exists between the predicted and experimental results. A comparison of Figures 8 and 12 reveals that the predicted surface temperature is approximately equal to the area-averaged temperature in the boundary layer, except in the leading edge region. Figure 12 shows that two-dimensional simulations can be used to provide guidance as to when and where rotor surface temperatures exceed allowable limits, provided an averaged temperature across the boundary layer is examined. This is an important finding which shows that costly and time consuming three-dimensional simulations of hot streak migration may not need to be executed to determine if rotor pressure surface burning is likely. Further investigation is required to determine if this manner of examining average viscous layer temperatures is reliable and applicable to other flow conditions and geometries.

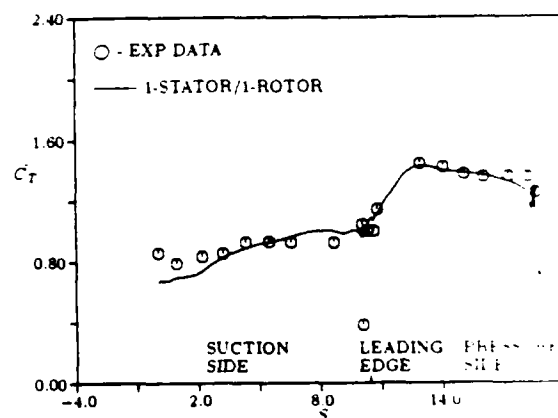


Figure 12: Predicted and experimental rotor surface temperatures - C_T

CONCLUSIONS

A numerical investigation has been performed to determine if two-dimensional stator/rotor/hot streak interaction simulations can provide reliable warnings to turbine designers as to *when* and *where* rotor surface temperatures exceed allowable limits. During this investigation, the results from an unsteady 1-stator/1-rotor/1-hot streak Navier-Stokes simulation were compared with new experimental data taken from a turbine stage which included a planar hot streak introduced at the stator inlet. The predicted and experimental rotor surface temperature distributions show close agreement, provided the proper correlation is made between the experimental CO_2 concentrations and the numerically predicted temperatures. Thus, for certain hot streak shapes, two-dimensional numerical procedures can be used as accurate and efficient tools by designers attempting to optimize cooling systems.

Future work will focus on developing improved techniques for comparing numerically predicted temperature distributions with experimental data. Based on the agreement between the current numerical results with the available experimental data, another investigation will be performed which uses the two-dimensional Navier-Stokes procedure to identify the effects of rotor inlet relative flow angle and boundary layer thickness on hot streak migration and rotor pressure surface heating.

ACKNOWLEDGEMENTS

This work was supported by the United Technologies Research Center under the Corporate Research Program. The authors appreciate the helpful discussions with Robert Dring and Dave Joslyn of the United Technologies Research Center.

REFERENCES

- Baldwin, B. S. and Lomax, H., 1978, "Thin-Layer Approximation and Algebraic Model for Separated Turbulent Flows," AIAA Paper 78-257.
- Butler, T. L., Sharma, O. P., Joslyn, H. D., and Dring, R. P., 1989, "Redistribution of an Inlet Temperature Distortion in an Axial Flow Turbine Stage," *Journal of Propulsion and Power*, Vol. 5, pp.64-71.
- Chakravarthy, S. and Osher, S., 1982, "Numerical Experiments with the Osher Upwind Scheme for the Euler Equations," AIAA Paper 82-0975.
- Dorney, D. J., Davis, R. L., Edwards, D. E., and Madavan, N. K., 1990, "Unsteady Analysis of Hot Streak Migration in a Turbine Stage," AIAA Paper 90-2354, also accepted for publication in the *Journal of Propulsion and Power*.
- Dring, R. P., Joslyn, H. D., Hardin, L. W., and Wagner, J. H., 1982, "Turbine Rotor-Stator Interaction," *Journal of Engineering for Power*, Vol. 104, pp.729-742.
- Krouthen, B., and Giles, M., 1988, "Numerical Investigation of Hot Streaks in Turbines," AIAA Paper 88-3015.

Madavan, N. K., Rai, M. M., and Gavali, S., 1989, "Grid Refinement Studies of Turbine Rotor-Stator Interaction," AIAA Paper 89-0325.

Rai, M. M., 1985, "An Implicit, Conservative, Zonal-Boundary Scheme for Euler Equation Calculations," AIAA Paper 85-0488.

Rai, M. M. and Madavan, N. K., 1988, "Multi-Airfoil Navier-Stokes Simulations of Turbine Rotor-Stator Interaction," AIAA Paper 88-0361.

Rai, M. M., 1989, "Three-Dimensional Navier-Stokes Simulations of Turbine Rotor-Stator Interaction," *Journal of Propulsion and Power*, Vol. 5, No. 3, pp.307-319.

Rai, M. M. and Dring, R. P., 1990, "Navier-Stokes Analyses of the Redistribution of Inlet Temperature Distortions in a Turbine," *Journal of Propulsion and Power*, Vol. 6, No. 3, pp.276-282.

Sharma, O. P., Pickett, G. F., and Ni, R. H., 1990, "Assessment of Unsteady Flows in Turbines," ASME Paper 90-GT-150.

Takahashi, R. and Ni, R. H., 1990, "Unsteady Euler Analysis of the Redistribution of an Inlet Temperature Distortion in a Turbine," AIAA Paper 90-2262.

Navier-Stokes Analysis of Turbine Blade Heat Transfer and Performance

Daniel J. Dorney*

and

Roger L. Davis†

United Technologies Research Center
East Hartford, CT

Summary

A three-dimensional Navier-Stokes analysis of heat transfer and aerodynamic performance is presented for a low speed linear turbine cascade. The numerical approach used in this analysis consists of an alternate-direction, implicit, approximate-factorization, time-marching technique. An objective of this investigation has been to establish the computational grid density requirements necessary to accurately predict blade surface and endwall heat transfer, as well as the exit plane aerodynamic total pressure loss and flow angle distributions. In addition, a study has been performed to determine a viable implementation strategy for the three-dimensional modelling of transition and turbulence in the turbine blade passage. Results are presented which demonstrate that the present procedure can accurately predict 3-D turbine blade heat transfer as well as the absolute level and spanwise distribution of aerodynamic performance quantities.

List of Symbols

a	- Speed of sound
c_p	- Specific heat ratio at constant pressure
e	- Specific energy
e_t	- Total energy
k	- Thermal conductivity
L	- Reference length (2.54 cm)
M	- Mach number
P	- Static pressure
Pr	- Prandtl number
P_T	- Stagnation pressure
q	- Heat flux
Re	- Free stream inlet reference Reynolds number
T	- Static temperature
u	- x component of velocity
v	- y component of velocity
w	- z component of velocity
λ	- Second coefficient of viscosity
μ	- First coefficient of viscosity
ρ	- Density
τ	- Shear stress

Subscripts

i	- Inviscid
L	- Laminar quantity
t	- Stagnation quantity
T	- Turbulent quantity
v	- Viscous
x, y, z	- First derivative with respect to x, y or z
xx, yy, zz	- Second derivative with respect to x, y or z
1	- Inlet quantity
2	- Exit quantity

*Associate Research Engineer, Theoretical & Computational Fluid Dynamics Group

†Senior Research Engineer, Theoretical & Computational Fluid Dynamics Group

Introduction

The accurate prediction of three-dimensional turbomachinery blade row heat transfer and aerodynamic performance, including total pressure loss and flow turning, remains a challenging task for most Navier-Stokes numerical procedures. The very large computational grid densities necessary to accurately resolve the viscous flow physics and properly convect the vorticity require computational resources which far exceed those available to most engineering facilities. Thus, in most instances, it has not been possible to produce grid-independent three-dimensional flow solutions for turbomachinery blade rows which ensure the accuracy required for reliable predictions.

The proper modelling of transition and turbulence within turbomachinery blade passages is also often compromised in order to reduce computational times to acceptable levels. The effects of turbulence in the flow are quite often modelled with an algebraic eddy viscosity correlation which has its basis in two-dimensional boundary layer data, even though the flow in a blade row passage has strong secondary and occasional reversed flows. The modelling of transition in most Navier-Stokes approaches is practically non-existent due to the lack of reliable correlations for three-dimensional internal blade row flows and due to the numerical instabilities caused by the unsteady movement of the transition region as the flow field develops. Unfortunately, it is unlikely that improvements in turbulence and transition modelling will improve beyond the current state-of-the-art for three-dimensional turbomachinery flows until Navier-Stokes procedures can affordably and reliably produce grid-independent solutions. Only then will researchers be able to separate out the turbulence modelling effects on the flow from those caused by truncation error and numerical viscosity.

Several investigations have been made recently in which three-dimensional Navier-Stokes procedures have been used to predict the heat transfer and/or aerodynamic performance of the Langston linear turbine cascade [1, 2]. Among these numerical investigations, Chan and Sheedy [3] have used a pressure correction method with a two equation ($k - \epsilon$) turbulence model to predict the losses in the Langston cascade for a thick (3.3 cm) inlet boundary layer. Their predicted results indicate the numerical procedure is very sensitive to spanwise computational grid density. Even the use of comparatively fine computational grids, however, was not adequate to achieve the flow field resolution needed to accurately predict aerodynamic performance quantities. Hah [4, 5] has also used a pressure correction technique with a two equation ($k - \epsilon$) turbulence model to predict endwall Stanton numbers [4] and losses as a function of axial distance [5] for the Langston cascade with a thick inlet boundary layer. The predicted endwall Stanton numbers show fair agreement with the experimental data, but it is unclear if a sufficiently fine computational grid was used to attain grid independent solutions. Moore [6, 7] has used a pressure correction method with an algebraic turbulence model to predict losses and secondary flows for the Langston cascade with a thick inlet boundary layer. Lee and Knight [8] solved the thin layer Navier-Stokes equations using an approximate factorization technique and the two equation ($q - \omega$) turbulence model to study heat transfer for the Langston cascade with a thick inlet boundary layer. A portion of their

investigation focused on the effects of different grid topologies (H- and O-H grids) on the predicted heat transfer quantities. In their study, it was determined that grid topology, as well as computational grid density, can impact the predicted solutions.

The objective of the current investigation has been to provide guidance as to the computational grid density requirements which are necessary to produce reliable and accurate Navier-Stokes predictions of turbomachinery blade row flows. Simulations of transitional flow through the Langston cascade [1, 2] with a thin inlet boundary layer (0.41 cm) have been performed where the focus has been to conduct a computational grid refinement study to determine the computational grid density necessary to properly resolve surface heat transfer and aerodynamic performance quantities. As part of this investigation, a study was performed to determine a viable strategy for implementing an algebraic turbulence model for three-dimensional internal blade row flows and to determine the limitations of using an algebraic turbulence model on the accuracy of the exit plane distributions of total pressure loss and flow angle. Also, a brief study was conducted to demonstrate the importance of modelling laminar/turbulent transition for these flows.

Numerical Integration Procedure

The governing equations considered in this study are the time dependent, three-dimensional Navier-Stokes equations:

$$U_t + (F_t + F_v)_x + (G_t + G_v)_y + (H_t + H_v)_z = 0 \quad (1)$$

where

$$U = \begin{bmatrix} \rho \\ \rho u \\ \rho v \\ \rho w \\ e_t \end{bmatrix} \quad (2)$$

$$F_t = \begin{bmatrix} \rho u \\ \rho u^2 + P \\ \rho uv \\ \rho uw \\ (e_t + P)u \end{bmatrix} \quad F_v = - \begin{bmatrix} 0 \\ \tau_{xz} \\ \tau_{xy} \\ \tau_{xz} \\ \tau_{hx} \end{bmatrix} \quad (3)$$

$$G_t = \begin{bmatrix} \rho v \\ \rho uv \\ \rho v^2 + P \\ \rho vw \\ (e_t + P)v \end{bmatrix} \quad G_v = - \begin{bmatrix} 0 \\ \tau_{yx} \\ \tau_{yy} \\ \tau_{yz} \\ \tau_{hy} \end{bmatrix} \quad (4)$$

$$H_t = \begin{bmatrix} \rho w \\ \rho uw \\ \rho vw \\ \rho w^2 + P \\ (e_t + P)w \end{bmatrix} \quad H_v = - \begin{bmatrix} 0 \\ \tau_{zx} \\ \tau_{zy} \\ \tau_{zz} \\ \tau_{hz} \end{bmatrix} \quad (5)$$

where

$$\begin{aligned} \tau_{xx} &= 2\mu u_x + \lambda(u_x + v_y + w_z) \\ \tau_{xy} &= \mu(u_y + v_x) \\ \tau_{xz} &= \mu(u_z + w_x) \\ \tau_{yx} &= \tau_{xy} \\ \tau_{yy} &= 2\mu v_y + \lambda(u_x + v_y + w_z) \end{aligned}$$

$$\begin{aligned} \tau_{yz} &= \mu(v_z + w_y) \\ \tau_{zx} &= \tau_{xz} \\ \tau_{zy} &= \tau_{yz} \\ \tau_{zz} &= 2\mu w_z + \lambda(u_x + v_y + w_z) \\ \tau_{hx} &= u\tau_{xx} + v\tau_{xy} + w\tau_{xz} + \gamma\mu P_r^{-1}e_x \\ \tau_{hy} &= u\tau_{yx} + v\tau_{yy} + w\tau_{yz} + \gamma\mu P_r^{-1}e_y \\ \tau_{hz} &= u\tau_{zx} + v\tau_{zy} + w\tau_{zz} + \gamma\mu P_r^{-1}e_z \\ e &= \frac{P}{(\rho(\gamma - 1))} \\ e_t &= \rho e + \frac{\rho(u^2 + v^2 + w^2)}{2} \end{aligned} \quad (6)$$

For the present application, the second coefficient of viscosity is calculated using Stokes' hypothesis, $\lambda = -2/3\mu$. The equations of motion are completed by the perfect gas law.

The viscous fluxes are simplified by incorporating the thin layer assumption [9]. In the current study, viscous terms are retained in the direction normal to the hub surface (z-direction) and in the direction normal to the blade surface (y-direction). To extend the equations of motion to turbulent flows, an eddy viscosity formulation is used. Thus, the effective viscosity and effective thermal conductivity can be defined as:

$$\begin{aligned} \mu &= \mu_L + \mu_T \\ \frac{k}{c_p} &= \frac{\mu_L}{P_r} + \frac{\mu_T}{P_{r,T}} \end{aligned} \quad (7)$$

The turbulent viscosity, μ_T , is calculated using the Baldwin-Lomax [9] algebraic turbulence model. The specific techniques used to implement this model for three-dimensional flows in turbomachinery blade rows will be described below.

The numerical procedure for the three-dimensional analysis consists of a time marching, implicit, third-order spatially accurate, upwind, finite difference scheme. The inviscid fluxes are discretized using a combination of central, forward, and backward differences depending on the local eigenvalues of the flux Jacobians according to the scheme developed by Roe [10]. The viscous fluxes are calculated using standard central differences. The alternate direction, approximate-factorization technique of Beam and Warming [11] is used to compute the time rate changes in the primary variables. An inner Newton iteration can be used to increase stability and reduce linearization errors. For all cases investigated in this study, one Newton iteration was performed at each time step. Further details of the three-dimensional numerical technique can be found in Refs. [12, 13].

Grid Generation and Geometry

The three-dimensional Navier-Stokes analysis uses zonal grids to discretize the turbine flow field. A combination of O- and H-grid sections are generated at constant radial spanwise locations in the blade-to-blade direction extending upstream of the airfoil leading edge to downstream of the airfoil trailing edge. Algebraically generated H-grids are used in the regions upstream of the leading edge, downstream of the trailing edge and in the inter-blade region. The O-grid, which is body-fitted to the surface of the airfoil and generated using an elliptic equation solution procedure, is used to properly resolve the viscous flow in the blade passages and to easily apply the algebraic turbulence model. Computational grid lines within the O-grid are stretched in the blade-normal direction with a fine grid spacing at the wall. The combined H- and O- overlaid grid sections are stretched in the spanwise direction away from the hub and shroud regions with a fine grid spacing located adjacent to the hub and shroud.

Boundary Conditions

The theory of characteristics is used to determine the boundary conditions at the passage inlet and exit. For subsonic inlet flow, the total pressure, v and w velocity components and the downstream running Riemann invariant, $R_1 = u + \frac{2a}{\gamma-1}$, are specified while the upstream running Riemann invariant, $R_2 = u - \frac{2a}{\gamma-1}$, is extrapolated from the interior of the computational domain. For subsonic outflow the pressure ratio, P_2/P_{t1} , is specified while the v and w velocity components, entropy, and the downstream running Riemann invariant are extrapolated from the interior of the computational domain. Periodicity is enforced along the outer boundaries of the H-grids in the circumferential (θ) direction.

Dirichlet conditions, in which the time rate change in the vector U of Eq. (2) is set to zero, are imposed at the overlaid boundaries of the O- and H-grids. The flow variables of U at zonal boundaries are explicitly updated after each time step by interpolating values from the adjacent grid. Because of the explicit application of the zonal boundary conditions, large time steps may necessitate the use of more than one Newton iteration. The zonal boundary conditions are non-conservative, but for subsonic flow this should not affect the accuracy of the final flow solution.

No-slip boundary conditions are enforced at the hub and shroud endwalls of the turbine passage and along the surface of the airfoil. In addition, a specified heat flux or wall temperature distribution is held constant in time along the solid surfaces. In the present investigation a specified heat flux given by

$$q_{wall} = -k \frac{\partial T}{\partial n} \quad (8)$$

is prescribed over all solid surfaces at a level consistent with the experimental conditions. Upon discretizing Eq. 8 using a first order backward difference, a Neumann boundary condition arises which is held during the implicit sweep of lines normal to the surface. The implicit update of the solid boundary flow variables is followed by a second order accurate explicit update. Further information describing the implementation of the boundary conditions can be found in Refs. [12, 13, 14].

Turbulence/Transition Model

The Baldwin-Lomax [9] two-layer algebraic turbulence model is used to represent the turbulent eddy viscosity in the flow field. This turbulence model is based upon two-dimensional boundary layer data, and as such, is not well suited for corner flows such as those at the blade/endwall juncture. Previously, the treatment used to implement this turbulence model in the corner regions was the technique proposed by Hung and Buning [15, 16]. In this technique, the Baldwin-Lomax turbulence model is computed separately for each endwall and the blade surface. The mixing length in the corner region depends on the computational indices of a given node. For instance, consider the case when the J =constant computational lines run normal to the blade surface and the K =constant lines run normal to the endwall. For any computational node whose J -wise index is less than its K -wise index, the 'normal' distance is defined as the distance from the blade surface to the grid point and the 'parallel' distance is defined as the distance from the endwall to the grid point. The mixing length for the inner region of the boundary layer is then calculated as

$$l = 2sn/(s + n + \sqrt{s^2 + n^2}) \quad (9)$$

where s is the parallel distance and n is the normal distance. The eddy viscosity is then based on the flow variables along a computational grid line from the airfoil surface (normal direction) to the grid point under consideration. Likewise, for any computational node whose J -wise index is greater than its K -wise index,

the parallel distance is measured from the blade surface to the grid point and the normal distance is measured from the endwall to the grid point. The eddy viscosity is then based on the flow variables along a computational grid line from the endwall to the grid point. Two significant problems arise from this particular three-dimensional implementation of the Baldwin-Lomax turbulence model. First, the eddy viscosity distribution in the corner regions is discontinuous across the $J=K$ computational lines which can cause large gradients to occur in the velocity field. Secondly, this particular blending is highly dependent upon the computational grid density and stretching in both computational directions. It was determined, based upon numerical simulations, that the steady-state solution in the blade/endwall region was extremely sensitive to changes in the computational grid structure.

In the present investigation, a blending function has been used to smoothly vary the eddy viscosity distribution between the blade and endwall. Separate eddy viscosity distributions are computed for the blade and endwall surfaces along the computational lines which run normal to each surface respectively. The eddy viscosity in the corner flow regions is then computed based upon the following blending function according to the work of Vatsa and Wedan [17]:

$$\mu_T = \frac{d_b^2 \mu_{T_b} + d_{ew}^2 \mu_{T_{ew}}}{d_b^2 + d_{ew}^2} \quad (10)$$

where d_b is the distance from the blade surface to a given node, d_{ew} is the distance from the endwall surface to the node, and μ_{T_b} , $\mu_{T_{ew}}$ are the eddy viscosities computed from the blade and endwall flows, respectively. This type of blending greatly reduces the dependence of the eddy viscosity distribution on the computational grid and creates a smooth eddy viscosity distribution in the corner regions.

As will be shown below, results from a number of computations demonstrate the importance of correctly modelling transition of the flow from laminar to turbulent on the blade surface. In the present investigation in which turbine blade heat transfer is being predicted, the modelling of transition is essential for the accurate prediction of Stanton number distributions. In this study, transition was modelled using a prescribed location for the onset of transition. The onset of transition was varied as a function of span, with the endwalls assumed to be fully turbulent, and mid-span transition beginning at the 20% axial chord location on the suction surface according to the experimental data. Transition was assumed to occur as an instantaneous process. As will be discussed below, a means of accurately predicting transition especially in turbine blade rows clearly must be developed in order to reliably and accurately predict heat transfer.

Results

A set of viscous three-dimensional numerical simulations of flow through the Langston low speed turbine cascade with a thin inlet boundary layer (0.41 cm), including heat transfer and transition, have been performed and the predicted results compared to experimental data [1, 2]. The heat flux values at the endwall and airfoil surfaces were specified to be the same as in Ref. [2]. The inlet Mach number was set to $M_1 = 0.0917$ and the inlet flow angle was specified to be $\beta_1 = 44.7$ degrees. The inlet Reynolds number was set to $Re_1 = 25590$ per cm and the ratio of the exit static pressure to the inlet total pressure was fixed at $P_2/P_{t1} = 0.9847$ based on the experimental data.

A computational grid refinement study has been performed to establish the grid density required to produce essentially grid-independent solutions in both the blade-to-blade and spanwise directions. A combination of two- and three-dimensional simulations were performed to establish the required grid density and wall spacing in the blade-to-blade direction to accurately predict turbine blade heat transfer. As a result of the two-dimensional

Case	Grid Density stream × tang × span	Δy_{blade} (y^+)	$\Delta y_{endwall}$ (y^+)	Profile $\Delta P_T / P_T$	Total $\Delta P_T / P_T$	Profile β_2	Total β_2	Trns
1	H-70 × 31 × 25	0.00100	0.00300	0.20846	0.19065	27.96	27.34	yes
	O-101 × 31 × 25	(4.260)	(7.430)					
2	H-70 × 31 × 25	0.00010	0.00100	0.16102	0.18373	27.49	27.36	no
	O-101 × 31 × 25	(0.384)	(2.920)					
3	H-70 × 31 × 25	0.00010	0.00100	0.16100	0.18372	27.49	27.58	yes
	O-101 × 31 × 25	(0.379)	(2.751)					
4	H-70 × 31 × 51	0.00010	0.00010	0.14575	0.17271	27.67	27.38	yes
	O-101 × 31 × 51	(0.360)	(0.266)					
5	H-70 × 31 × 71	0.00010	0.00010	0.13898	0.17075	27.73	27.26	yes
	O-101 × 31 × 71	(0.351)	(0.266)					
6	H-70 × 31 × 91	0.00010	0.00010	0.13051	0.17064	27.75	27.25	yes
	O-101 × 31 × 91							
2-D	O-131 × 61	0.00002	—	0.12030	—	26.58	—	yes
	H-71 × 21	(0.059)	—					
EXPT	—	—	—	0.13000	0.17437	26.80	26.32	—

Table 1: Grid refinement study

simulations, it was determined that a computational grid consisting of 70 × 21 grid points in the H-grid and 131 × 61 grid points in the O-grid with an average wall spacing of 0.00002 ($y^+ = .059$) produced grid-independent solutions. Once this was established, a similar grid topology and density were used in the blade-to-blade direction for the three-dimensional simulations. The wall spacing adjacent to the airfoil surface was then refined during a series of three-dimensional simulations to insure the accuracy of the three-dimensional blade-to-blade solution. Finally, the spanwise computational grid was refined both in terms of endwall spacing and density until the exit total pressure loss and exit flow angle distributions remained unchanged and exhibited close agreement with the experimental data.

A summary of the cases executed during this investigation are given in Table 1. The columns labelled 'Total' in Table 1 indicate area-averaged values in the spanwise direction, while the columns labelled 'Profile' refer to mid-span values. The area-averaged values were calculated using trapezoidal integration and only the computational grid points at the experimental data locations were included in the integration (a total of 13 locations for the half-span) in order to be consistent with the experimental area-averaged exit loss and flow angle values. The column labelled 'Trns' indicates whether or not transition was modelled. Since the geometry was symmetric about the mid-span, the numerical simulations were performed for only the half-span and a symmetry boundary condition was used along the symmetry plane. The spanwise grid densities given in Table 1 are for the half-span geometry. Figure 1, which illustrates the 'Total' exit flow angle and total pressure loss (see Eq. 13) values as a function of grid point density, demonstrates that a half-span grid-independent solution was obtained with approximately 450,000 grid points. Except where noted, the predicted results shown below are for this fine grid (Case 6) solution.

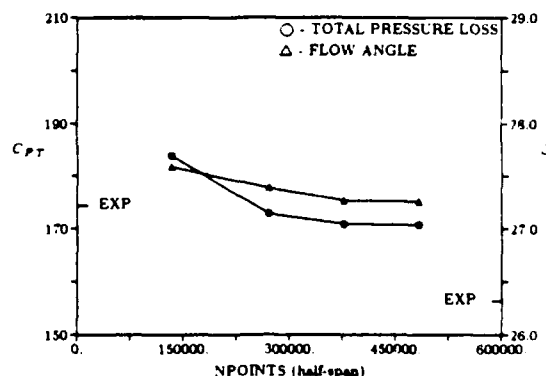


Figure 1: Exit flow angle and total pressure loss as a function of grid point density

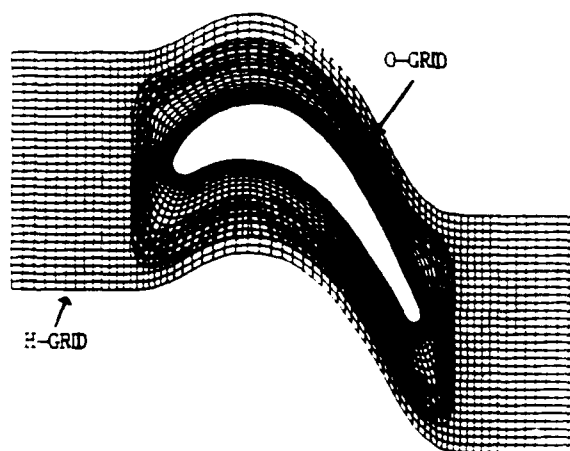


Figure 2: Blade-to-blade computational grid for Langston cascade

Figure 2 illustrates an example of the blade-to-blade computational grid used in the numerical simulations. Planes of blade-to-blade computational grids such as shown in Figure 2 are stacked in the spanwise direction to create the discretized geometry. Computational grid lines are clustered adjacent to the airfoil surface and endwall to properly resolve the viscous flow.

Figure 3 illustrates the predicted fine grid (Case 6) and experimentally measured pressure coefficient distributions along the surface of the airfoil at the 2.9, 12.5, 25.0, and 50.0% span locations, where the pressure coefficient is defined as:

$$C_p = \frac{2(P - P_1)}{\rho U_1^2} \quad (11)$$

and U_1 is the total inlet velocity. Experimental data was taken on two separate blades in the cascade and both sets of data are presented for each spanwise location. There is close agreement between the predicted results and the experimental data for the entire span of the cascade. In both the predicted results (Cases 4-6 in Table 1) and the experimental data the effects of the endwall secondary flow on the pressure distribution are visible on the suction surface of the airfoil near the trailing edge at 12.5% span. This phenomenon was not present in the coarser grid calculations (Cases 1-3).

The predicted and experimental [2] endwall static pressure coefficient contours are illustrated in Figures 4 and 5, respectively. Comparison of the two figures show that the predicted results and experimental data agree very well. Both figures show a pressure "island", corresponding the minimum pressure point, located on the suction surface at approximately 60% axial chord.

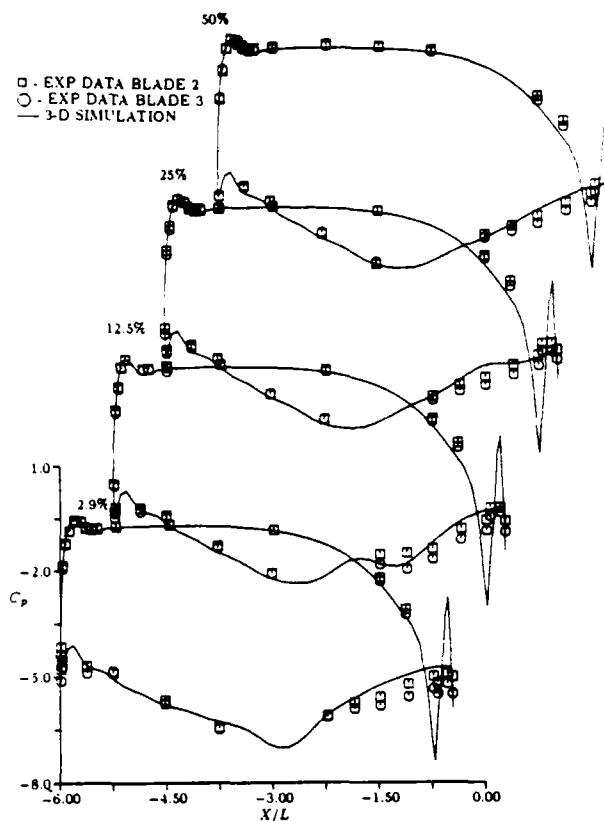


Figure 3: Airfoil surface static pressure coefficient distributions 22

The predicted static pressure coefficient contours for the suction and pressure surfaces of the airfoil are shown in Figures 6 and 7, while the experimental contours for both surfaces are shown in Figures 8 and 9, respectively. It is important to note that Figures 6 and 7 are three-dimensional renderings of the airfoil surface, while Figures 8 and 9 are two-dimensional projections of the airfoil surface. There is good agreement between the predicted results and experimental data on both surfaces of the airfoil. The static pressure island associated with the minimum pressure point, located at 38% axial chord on the suction surface, is shown in both the predicted and experimental results. The effects of the endwall boundary layer are visible in Figures 6 and 8 just downstream of the mid-axial chord location. In both the predicted results and the experimental data, the static pressure changes very little for the first 50% axial chord of the pressure surface (see Figures 7 and 9), then decreases very rapidly as the flow accelerates near the trailing edge.

The predicted limiting streamlines for the suction surface of the airfoil are shown in Figure 10. Limiting streamlines obtained experimentally using surface flow visualization techniques are included for comparison in Figure 11. The predicted limiting streamlines (Figure 10) show close agreement with the experimental data. The flow in the mid-span region of the suction surface is two-dimensional, while the flow in the endwall region is highly three-dimensional. A separation streamline forms at the airfoil leading edge in the endwall region and extends spanwise to approximately the 25% span position at the trailing edge. As the flow moves towards the exit of the blade passage, it is forced towards mid-span by the endwall secondary flow. The predicted pressure surface limiting streamlines are shown in Figure 12. The corresponding experimental pressure surface limiting streamlines are presented in Figure 13. The leading edge stagnation line is well illustrated in Figure 12 and it is evident from both the predicted and experimental limiting streamlines that the flow on the pressure surface is predominantly two-dimensional in nature.

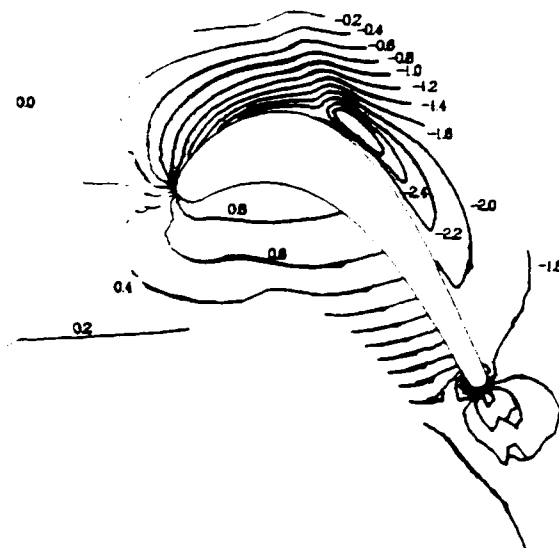


Figure 4: Predicted 3-D endwall static pressure coefficient contours

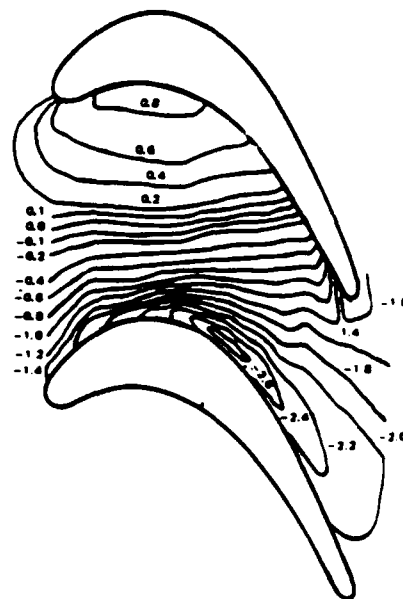


Figure 5: Experimental 3-D endwall static pressure coefficient contours

The predicted endwall limiting streamlines from the fine grid simulation are shown in Figure 14, while the experimental endwall limiting streamlines are shown in Figure 15. In both Figures 14 and 15, a saddle point is evident near the pressure surface leading edge of the airfoil. In the numerical simulation, the saddle point location is predicted somewhat further upstream than that observed in the experiment. This may indicate that the predicted endwall boundary layer is slightly too thick. In Reference [2] it was demonstrated that the location of the saddle point moves upstream as the endwall boundary layer is thickened. In both Figures 14 and 15, the flow in the leading edge region moves onto the suction side of the passage and intersects the suction surface near the minimum pressure point. The flow on the pressure side of the passage migrates towards the suction surface, intersecting it in the region downstream of the minimum pressure point.

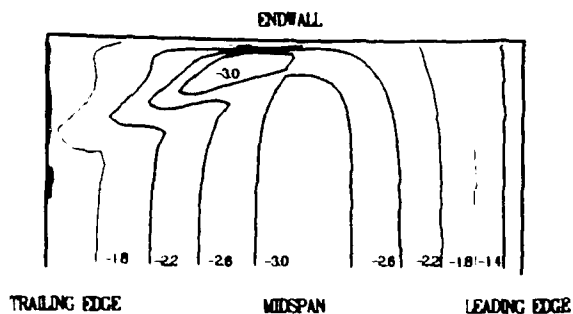


Figure 6: Predicted suction surface static pressure coefficient contours

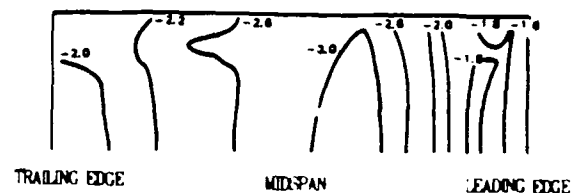


Figure 8: Experimental suction surface static pressure coefficient contours

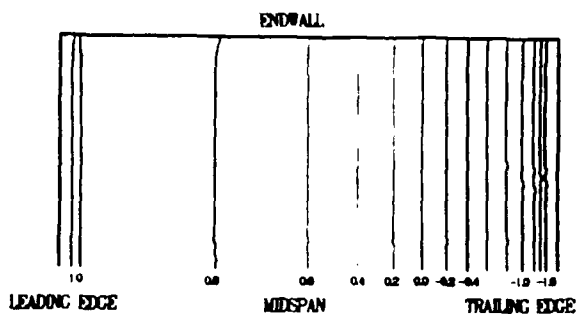


Figure 7: Predicted pressure surface static pressure coefficient contours

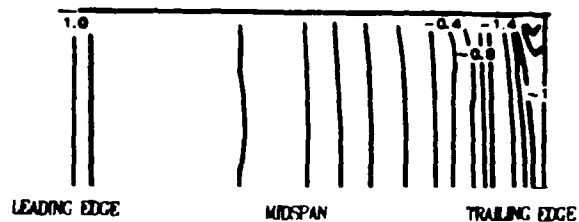


Figure 9: Experimental pressure surface static pressure coefficient contours

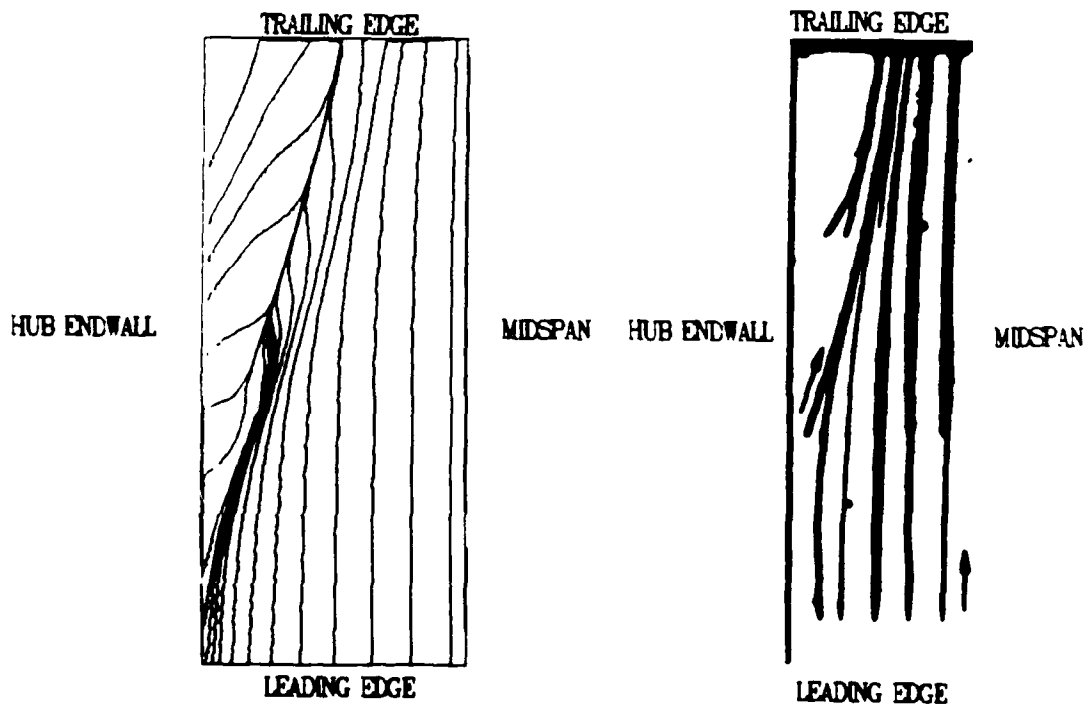


Figure 10: Predicted suction surface limiting streamlines



Figure 11: Experimental suction surface limiting streamlines

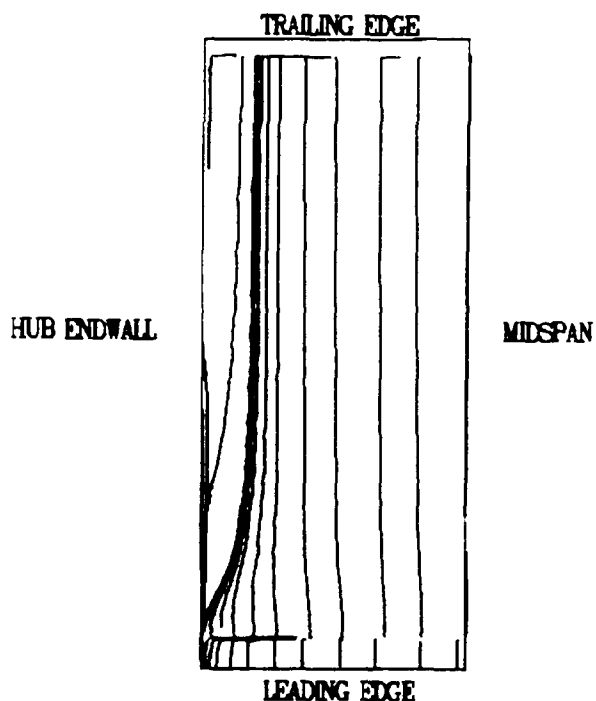


Figure 12: Predicted pressure surface limiting streamlines

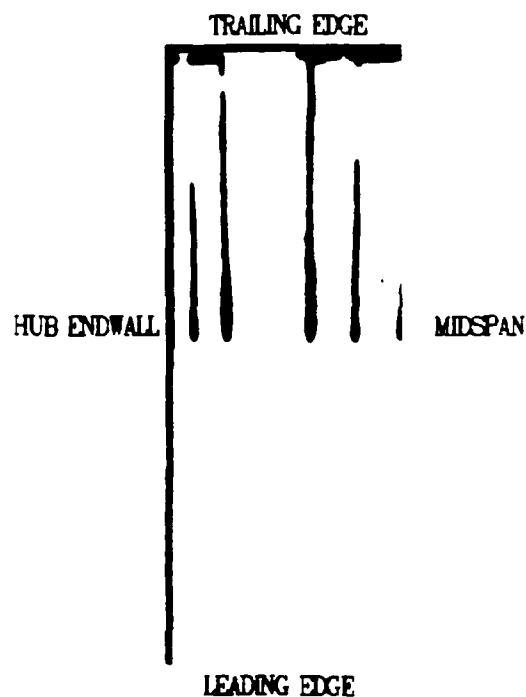


Figure 13: Experimental pressure surface experimental limiting streamlines

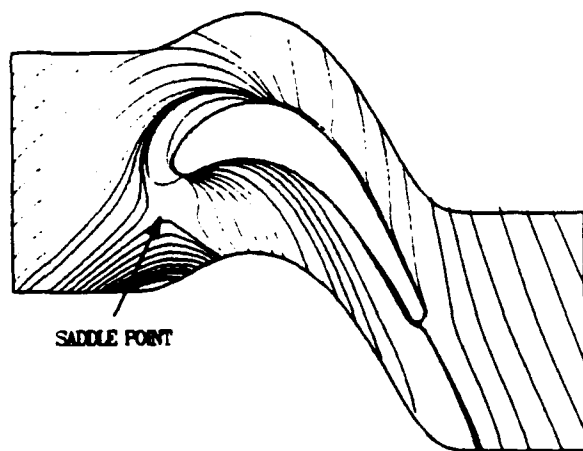


Figure 14: Predicted endwall limiting streamlines

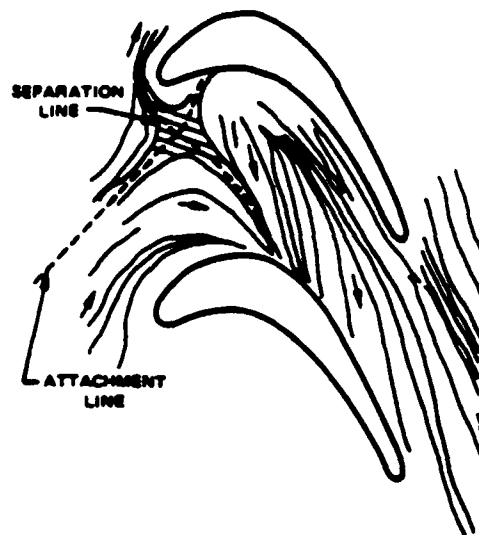


Figure 15: Experimental endwall limiting streamlines

To assess the ability of the present Navier-Stokes analysis to predict heat transfer, the Stanton number was calculated along the surface of the airfoil and compared with the experimental data [2]. The Stanton number is defined as:

$$St = \left(\frac{\partial h}{\partial n} \right) / (Re Pr (h_{aw} - h_w)) \quad (12)$$

and n is the normal distance from the wall, h_{aw} is the adiabatic enthalpy at the wall, and h_w is the enthalpy at the wall. Figure 16 compares the predicted suction surface mid-span Stanton number distributions obtained with and without transition, the predicted results from the two-dimensional simulation, and the experimental data. The fully turbulent calculation overpredicts the Stanton number in the first 25% of the axial chord, demonstrating the importance of modelling transition. As discussed earlier, mid-span

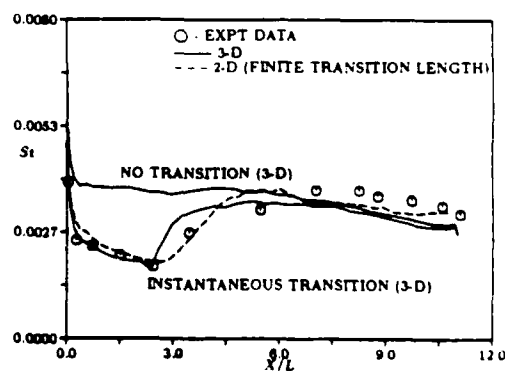


Figure 16: Mid-span suction surface Stanton number distributions

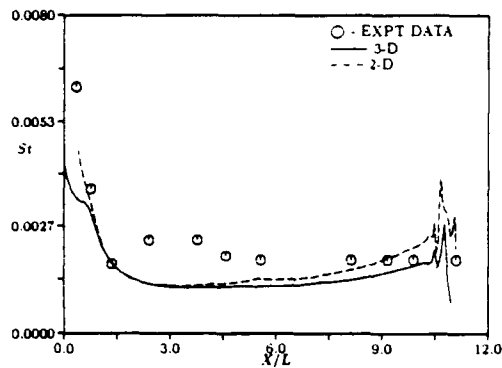


Figure 17: Mid-span pressure surface Stanton number distributions

transition was prescribed, according to the experimental data, to be instantaneous at the 25% axial chord position. The effects of transition are evident from the rapid increase in the Stanton number at the 25% axial chord location. The Stanton number is predicted very well ahead of transition but is slightly underpredicted aft of the transition point. It has been found, based upon a number of two-dimensional simulations, that this small discrepancy is due to the instantaneous transition model currently used in the three-dimensional procedure. Very good agreement was found to exist between the predicted Stanton number distribution and the experimental data in the two-dimensional simulations when transition was modeled over a region extending between 25 - 60% axial chord (see Figure 16).

A comparison of the predicted three-dimensional mid-span pressure surface Stanton number distribution with the experimental data is presented in Figure 17. The three-dimensional predicted results demonstrate only fair agreement with the experimental data. A series of two-dimensional simulations were performed to determine if the differences between the predicted Stanton number and the experimental data near the 25% axial chord location was due to transition, similar to the suction surface. The results from these two-dimensional simulations showed that transition had little effect on the pressure side Stanton number distribution in this region of the flow. Further investigation is required to determine the contributing factor of this difference.

The predicted three-dimensional fine grid suction surface Stanton number contours are shown in Figure 18. The experimental suction surface Stanton number contours are illustrated in Figure 19. The predicted results demonstrate good quantitative agreement with the experimental data, except along the hub endwall downstream of the separation streamline, where the experimental data indicates increased amounts of heat transfer. In Figure 18, the variation of the transition location with span is apparent in the leading edge endwall regions. Both the predicted results and the experimental data indicate enhanced heat transfer at the airfoil leading edge in the endwall regions and downstream of the endwall separation line.

Figures 20 and 21 illustrate the predicted fine grid and experimental Stanton number contours for the pressure surface. The predicted Stanton number distribution shows close agreement with the experimental data. Both the predicted results and the experimental data reveal much less heat transfer taking place on the pressure surface, as indicated by smaller values of the Stanton number.

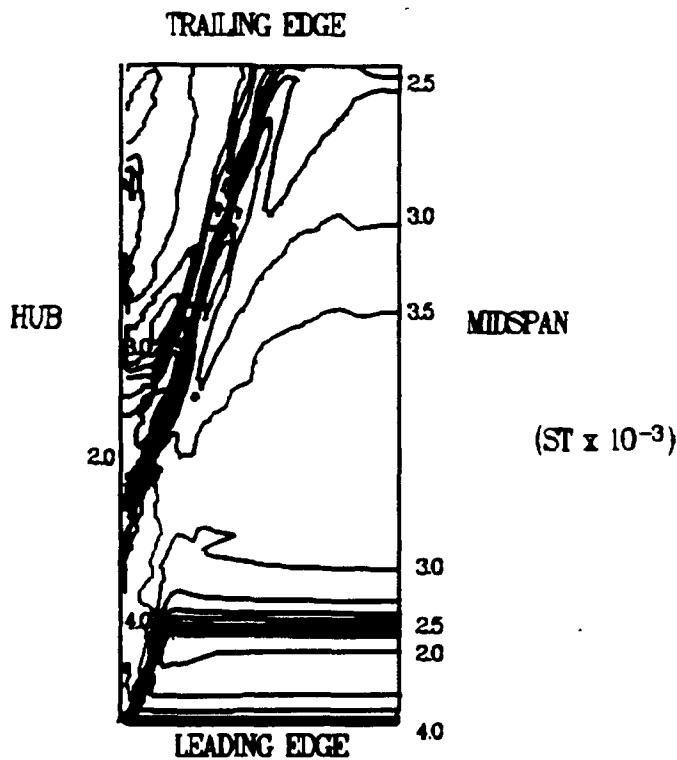


Figure 18: Predicted suction surface Stanton number contours

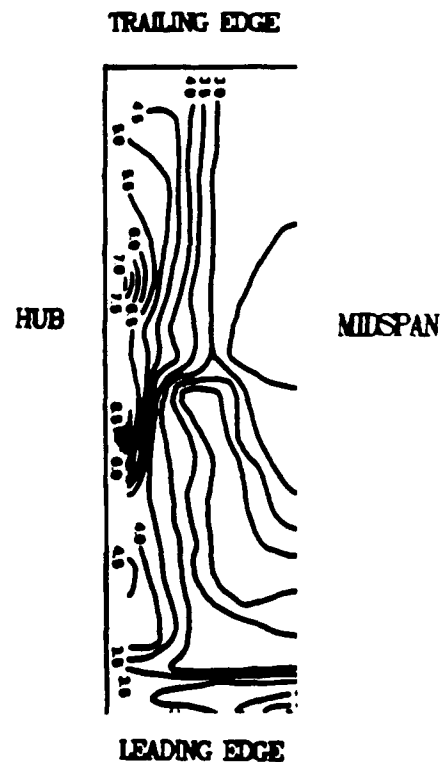


Figure 19: Experimental suction surface Stanton number contours

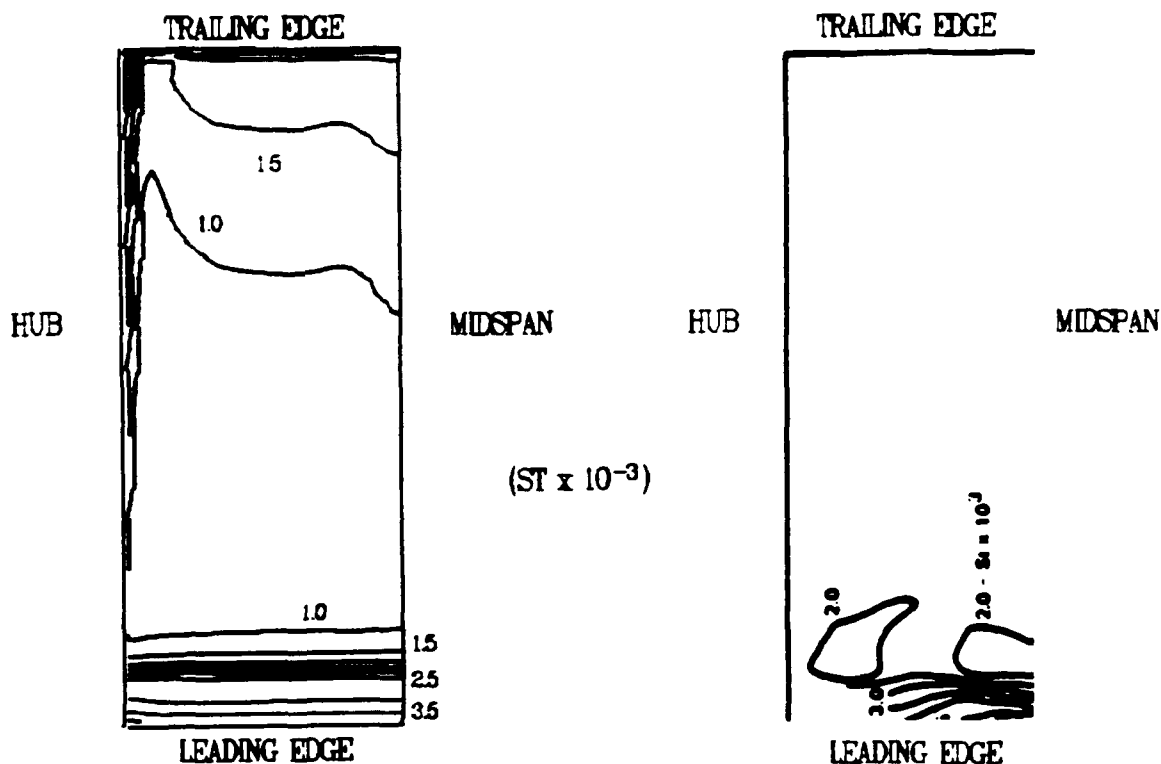


Figure 20: Predicted pressure surface Stanton number contours

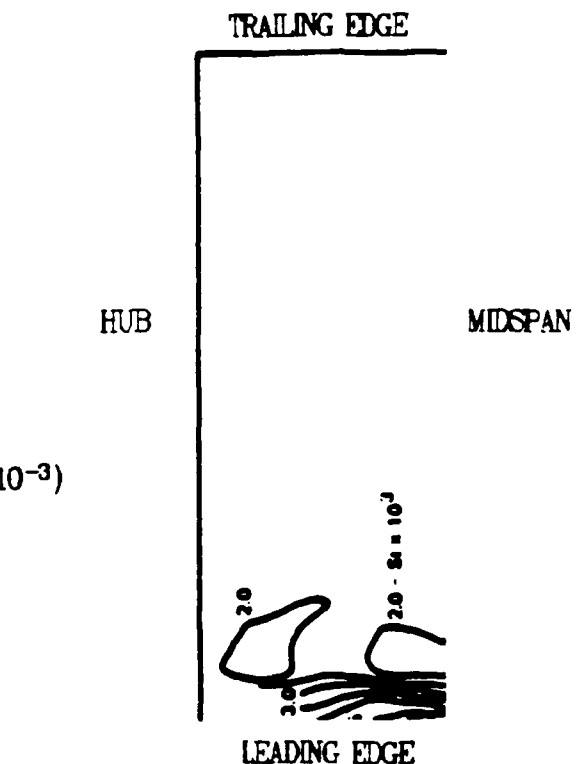


Figure 21: Experimental pressure surface Stanton number contours

Figures 22 and 23 present the predicted fine grid and experimental Stanton number contours for the endwall. In both the predicted results and the experimental data, the lowest values of the endwall Stanton number are located on the pressure surface, beginning just downstream of the saddle point and extending to the trailing edge. In both figures, a region of increased heat transfer is located near the suction surface leading edge and in the vicinity of the minimum pressure point on the suction surface.

In the wake region, discrepancies exist between the predicted results and the experimental data. The predicted results indicate a small amount of heat transfer in the wake region, while the experimental data indicates larger amounts of heat transfer. These discrepancies are probably due to the use of an O-grid around the airfoil, which precludes the use of wake modelling in the algebraic turbulence model. Other than in the wake region, the predicted results show good agreement with the experimental data.

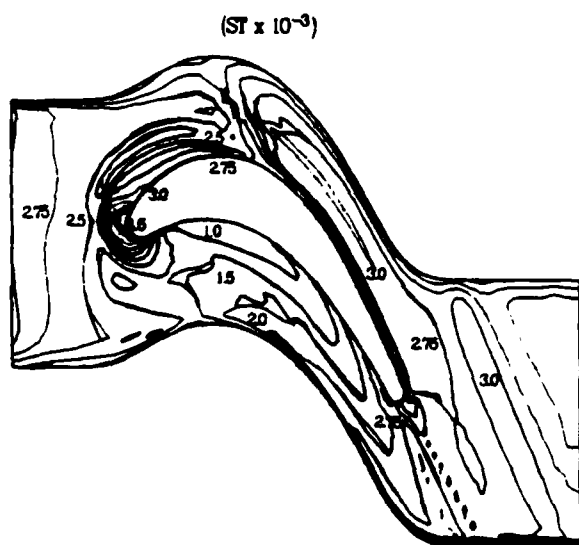


Figure 22: Predicted endwall Stanton number contours

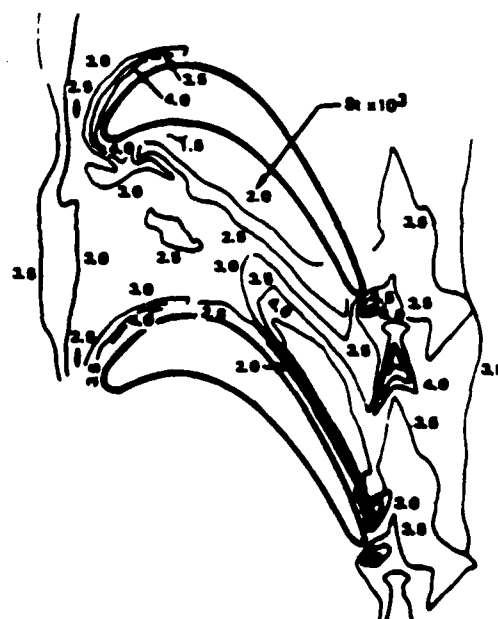


Figure 23: Experimental endwall Stanton number contours

Conclusions

A three-dimensional, implicit, upwind Navier-Stokes procedure has been used to predict heat transfer and aerodynamic performance quantities in the Langston cascade for a thin inlet boundary layer. A grid resolution study has been performed which indicates that approximately 900,000 (full span) computational grid points are required for a single turbomachinery blade row to produce grid-independent solutions for flows at Reynolds numbers typical of those in gas turbine engines. In addition, this study has shown that overall aerodynamic turbomachinery blade row performance can be predicted within 2% using these fine computational grids with the Baldwin-Lomax algebraic turbulence model. Also, the importance of modelling transition from laminar to turbulent flow within the blade passage for the accurate prediction of heat transfer is demonstrated. Clearly, further progress in reducing the computational time required for three-dimensional Navier-Stokes procedures is required to enable reliable and affordable grid-independent solutions for turbomachinery blade row flows. This capability is required before major improvements in turbulence modelling can be made and three-dimensional heat transfer and aerodynamic performance quantities can be routinely and accurately predicted.

Acknowledgements

This work was supported by the Naval Air Systems Command under NAVAIR contract N00140-88-0677 from the office of George Derderian with Raymond Shreeve of the Naval Post Graduate School acting as technical monitor and the United Technologies Research Center under the Corporate Research Program. The three-dimensional simulations performed during this investigation were performed on the NAS Numerical Aerodynamic Simulation CRAY-2 supercomputer. The authors would like to thank Man Mohan Rai and Linda Haines of the NASA Ames Research Center for assistance in computational aspects of this investigation. The authors appreciate the helpful discussions with Om Sharma of Pratt & Whitney and Mike Blair and Bob Dring of the United Technologies Research Center concerning interpretation of the experimental results.

References

- [1] Langston, L. S., Nice, M. L., and Hooper, R. M., "Three-Dimensional Flow Within a Turbine Cascade Passage," ASME Paper No. 76-GT-50, March, 1976.
- [2] Graziani, R. A., Blair, M. F., Taylor, J. R., and Mayle, R. E., "An Experimental Study of Endwall and Airfoil Surface Heat Transfer in a Large Scale Turbine Blade Cascade," *Journal of Engineering for Power*, Vol. 102, No. 2, April, 1980, pp.257-267.
- [3] Chan, D. C. and Sheedy, K. P., "Turbulent Flow Modeling of a Three-Dimensional Turbine," AIAA Paper 90-2124, July, 1990.
- [4] Hah, C., "Numerical Study of Three-Dimensional Flow and Heat Transfer Near the Endwall of a Turbine Blade Row," AIAA Paper 89-1689, June, 1989.
- [5] Hah, C., "A Navier-Stokes Analysis of Three-Dimensional Turbulent Flows Inside Turbine Blade Rows at Design and Off-Design Conditions," *Journal of Engineering for Gas Turbines and Power*, Vol. 106, April, 1984, pp. 421-429.
- [6] Moore, J. and Moore, J. G., "Performance Evaluation of Linear Turbine Cascades Using Three-Dimensional Viscous Flow Calculations," *ASME Journal of Engineering for Gas Turbines and Power*, October, 1985.
- [7] Moore, J. and Ransmayr, A., "Flow in a Turbine Cascade: Part I - Losses and Leading Edge Effects," *ASME Journal of Engineering for Gas Turbines and Power*, Vol. 106, April, 1984, pp. 400-408.
- [8] Lee, D. and Knight, C. J., "Evaluation of an O-H Grid Formulation for Viscous Cascade Flows," AIAA Paper 89-0207, January, 1989.
- [9] Baldwin, B. S. and Lomax, H., "Thin-Layer Approximation and Algebraic Model for Separated Turbulent Flows," AIAA Paper 78-257, January, 1978.
- [10] Roe, P. L., "Approximate Riemann Solvers, Parameter Vectors, and Difference Schemes," *Journal of Computational Physics*, Vol. 43, pp.357-372, 1981.
- [11] Beam, R. M. and Warming, R. F., "An Implicit Factored Scheme for the Compressible Navier-Stokes Equations," AIAA Paper 77-645, 1977.
- [12] Rai, M. M., "Three-Dimensional Navier-Stokes Simulations of Turbine Rotor-Stator Interaction," *Journal of Propulsion and Power*, Vol. 5, May-June, 1989.
- [13] Rai, M. M. and Madavan, N. K., "Multi-Airfoil Navier-Stokes Simulations of Turbine Rotor-Stator Interaction," AIAA Paper 88-0361, 1988.
- [14] Rai, M. M., "An Implicit, Conservative, Zonal-Boundary Scheme for Euler Equation Calculations," AIAA Paper 85-0488, 1985.
- [15] Hung, C. M. and Buning, P. G., "Simulation of Blunt-Fin Induced Shock Wave and Turbulent Boundary Layer Interaction," AIAA Paper 84-0457, January, 1984.
- [16] Hung, C. M. and McCormack, R. W., "Numerical Solution of Three-Dimensional Wave and Turbulent Boundary Layer Interaction," AIAA Paper 78-161, January, 1978.
- [17] Vatsa, V. N. and Wedan, B. W., "Navier-Stokes Solutions for Transonic Flow Over a Wing Mounted in a Wind Tunnel," AIAA Paper 88-0102, January, 1988.
- [18] Dhawan, S. and Narasimha, R., "Some Properties of Boundary Flow During Transition from Laminar to Turbulent Motion," *Journal of Fluid Mechanics*, Vol. 3, 1958, pp.418-436.
- [19] Johnson, D. A. and King, L. S., "A Mathematically Simple Turbulence Closure Model for Attached and Separated Turbulent Boundary Layers," *AIAA Journal*, Vol. 23, No. 11, November 1985, p. 1684.